

A Low Temperature Kinetic Study of the C(³P) + CH₃OCH₃ Reaction. Rate constants, H-atom Product Yields and Astrochemical Implications

Kevin M. Hickson,^{1,*} Jean-Christophe Loison,¹ and Valentine Wakelam²

¹Institut des Sciences Moléculaires ISM, CNRS UMR 5255, Univ. Bordeaux, 351 Cours de la Libération, F-33400, Talence, France

²Laboratoire d'astrophysique de Bordeaux, CNRS, Univ. Bordeaux, B18N, allée Geoffroy Saint-Hilaire, F-33615 Pessac, France

Abstract

Atomic carbon in its ground electronic state, C(³P), is expected to be present at high abundances during the evolution of dense molecular clouds. Consequently, its reactions with other interstellar species could have a strong influence on the chemical composition of these regions. Here, we report the results of an investigation of the reaction between C(³P) and dimethylether, CH₃OCH₃, which was recently detected in dark cloud TMC-1. Experiments were performed to study the kinetics of this reaction using a continuous supersonic flow reactor employing pulsed laser photolysis and pulsed laser induced fluorescence for atomic radical generation and detection respectively. Rate constants for this process were measured between 50 K and 296 K, while additional measurements of the product atomic hydrogen yields were also performed over the 75-296 K range. To better understand the experimental results, statistical rate theory was used to calculate rate constants over the same temperature range and to provide insight on the major product channels. These simulations, based on quantum chemical calculations of the ground triplet state of the C₃H₆O molecule, allowed us to obtain the most important features of the underlying potential energy surface. The measured rate constant increases as the temperature falls, reaching a value of $k_{C+CH_3OCH_3} = 7.5 \times 10^{-11} \text{ cm}^3 \text{ s}^{-1}$ at 50 K, while the low measured H-atom yields support the theoretical prediction that the major reaction products are CH₃ + CH₃ + CO. The effects of this reaction on the abundances of interstellar CH₃OCH₃ and related species were tested using a gas-grain model of dense interstellar clouds, employing an expression for the rate constant, $k(T) = \alpha(T/300)^\beta$, with $\alpha = 1.27 \times 10^{-11}$ and $\beta = -1.01$. These simulations predict that the C(³P) + CH₃OCH₃ reaction decreases gas-phase CH₃OCH₃ abundances by more than an order of magnitude at early and intermediate cloud ages.

Keywords Chemical kinetics, gas-phase, low temperature, ab initio calculations, astrochemistry.

Introduction

Carbon is the fourth most abundant element after hydrogen, helium and oxygen and is present throughout the Universe as an isolated species, C in both its neutral and ionic forms, as well as being incorporated into numerous organic type molecules. In the interstellar medium (ISM), the gravitational collapse of diffuse clouds of gas and dust forming denser, darker regions is accompanied by a transformation of the underlying composition. This occurs due to a change in the physical conditions, from regions where photons dominate so that the chemistry involves atoms and ions, to regions where photons play a much less important role and the chemistry is dominated by reactions between neutral species. Under these conditions, elemental carbon initially present as C^+ due to its low ionization potential is rapidly converted to neutral atomic carbon in its ground electronic state, $C(^3P)$. Indeed, observations of $C(^3P)$ atoms towards dense molecular clouds such as TMC-1,¹ OMC-1^{2,3} and Barnard 5⁴ through its fine structure transitions in the submillimeter-wave range (492.162 and 809.345 GHz) clearly indicate that neutral atomic carbon is present within these clouds at high abundance levels, coexisting alongside major reservoir species of C and O such as CO. As astrochemical models⁵ predict that neutral atomic carbon abundances are high (10^{-4} with respect to H_2) during the early stages of cloud evolution, it is important to evaluate the importance of the reactions of $C(^3P)$ atoms with other interstellar species to examine their effects on the overall composition of these regions. Indeed, the dense ISM is home to a wide variety of organic molecules ranging from simple diatomic radicals such as CH to large species such as C_{70} .⁶ While there are many previous studies of the reactivity of $C(^3P)$ with unsaturated hydrocarbons⁷⁻¹⁶, there are relatively few studies of its reactions with organic molecules containing other functional groups^{17,18} such as those found in complex organic molecules (COMs). COMs, arbitrarily defined as carbon bearing molecules containing six or more atoms¹⁹ have been detected in a wide variety of interstellar environments ranging from warmer regions such as protostellar envelopes,²⁰ hot cores²¹ and hot corinos²² to cold objects such as prestellar cores.²³ Among these COMs, dimethyl ether, CH_3OCH_3 , was first detected towards the Orion molecular cloud in 1974 by Snyder et al.²⁴ Although it has since been observed in numerous “warm” interstellar objects including low,²⁵ intermediate²⁶ and high mass star forming regions,²⁷ it is not restricted to these environments where ice sublimation is expected to play an important role by boosting gas-phase COM abundances. Indeed,

CH₃OCH₃ has been detected recently²⁸ in the prototypical dark cloud TMC-1 with an abundance of 2.5×10^{-10} with respect to H₂ and towards the prestellar core L1689B²³ with a similar abundance of a few 10^{-10} . In astrochemical databases such as the Kinetic Database for Astrochemistry (KIDA),²⁹ CH₃OCH₃ formation in the gas-phase occurs through only one dissociative electron recombination reaction at the present time, namely the CH₃OCH₄⁺ + e⁻ → CH₃OCH₃ + H reaction. The radiative association reaction CH₃O + CH₃ → CH₃OCH₃ + photon suggested by Balucani et al.³⁰ and the (CH₃)₂OH⁺ + NH₃ → CH₃OCH₃ + NH₄⁺ ion molecule reaction proposed by Skouteris et al.³¹ are not yet included in KIDA. Instead, CH₃OCH₃ is considered to be synthesized primarily on interstellar ices, by a range of processes including the sequential hydrogenation of simpler carbon and oxygen bearing molecules such as CH₃OH.³² Despite this, models typically underestimate the observed gas-phase CH₃OCH₃ abundances in the dense ISM either due to the difficulty of reinjecting these molecules into the gas-phase in sufficient quantities at such low temperatures (10 K or lower) or because important gas-phase or surface reactions are missing.

To improve our understanding of the interstellar chemistry of dimethyl ether, we performed an experimental and theoretical study of the C(³P) + CH₃OCH₃ reaction. On the experimental side, a supersonic flow apparatus has been employed to investigate the kinetics of this reaction over the 50-296 K range, coupled with pulsed laser photolysis and pulsed laser induced fluorescence for the production and detection of C(³P) atoms in the cold supersonic flow. In addition to the kinetic studies, measuring temperature dependent rate constants for this process, we have also measured those product channels leading to H-atom formation at room temperature and below. In conjunction with electronic structure calculations of the underlying potential energy surface, and a Rice Ramsperger Kassel Marcus (RRKM) master equation (ME) analysis of the major pathways, it has been possible to identify the major product channels of this reaction for astrochemical modeling purposes. Finally, the effects of the C(³P) + CH₃OCH₃ reaction on interstellar chemistry have been tested through an astrochemical modeling study employing both gas-phase and grain surface reactions.

The paper is organized as follows. The experimental and theoretical methods are described in sections 2 and 3 respectively, while the results of this work are presented in section 4. The astrochemical simulations and the implications of this study for interstellar dimethyl ether and related species are given in section 5, followed by our conclusions in section 6.

2 Experimental Methods

An existing continuous supersonic flow reactor was used to perform the experimental work described here.^{33,34} Subsequent modifications to the apparatus, particularly on the detection side, have allowed us to perform kinetic studies of the reactions of atomic radicals in both the ground ($\text{H}(^2\text{S}),$ ³⁵ $\text{C}(^3\text{P}),$ ³⁶ $\text{N}(^4\text{S})$ ³⁷) and excited ($\text{O}(^1\text{D}),$ ³⁸ $\text{N}(^2\text{D})$ ³⁹) electronic states. Here, convergent-divergent Laval type nozzles⁴⁰ were employed to produce supersonic flows of a specified carrier gas (Ar or N_2 in this instance) with the uniform temperature, density and velocity profiles required to study the kinetics of the $\text{C}(^3\text{P}) + \text{CH}_3\text{OCH}_3$ reaction below room temperature. As these flows typically persist for only a few tens of centimetres, such methods are generally applicable to the study of fast reactions only (i.e., with rate constants $> 10^{-12} \text{ cm}^3 \text{ s}^{-1}$). Three different nozzles were employed during this investigation to access four different low temperatures (one nozzle was used with both Ar and N_2), allowing flows with characteristic temperatures of 177 K, 127 K, 75 K and 50 K to be generated. The flow properties for each nozzle are summarized in Table 2 of Hickson et al.³⁶ The nozzle was mounted on a piston that could slide in and out of the reactor, allowing it to be positioned at a specified distance from the observation axis. For any particular nozzle this value corresponded to the maximum distance for which the flow conditions were considered to remain optimal. These characteristic distances were derived during earlier calibration experiments examining the variation of the supersonic flow impact pressure as a function of distance from a Pitot tube.³³ To perform experiments at room temperature (296 K), the nozzle was removed, while the flow velocity was decreased to eliminate pressure gradients within the chamber.

$\text{C}(^3\text{P})$ atoms were generated in situ during these experiments by the 266 nm pulsed (10 Hz) photolysis of trace amounts of tetrabromomethane (CBr_4) molecules in the supersonic flow. To carry these molecules into the reactor, a small fraction of the carrier gas was diverted into a vessel at room temperature containing CBr_4 crystals before rejoining the main flow upstream of the Laval nozzle reservoir. For any series of measurements at a given flow temperature, the pressure in the vessel was set to a fixed value by adjusting a needle valve at the outlet. Based on its saturated vapour pressure at room temperature (0.7 Torr), the CBr_4 concentration in the cold flow was estimated to be less than $2.6 \times 10^{13} \text{ cm}^{-3}$. Pulse energies of approximately of 30-38 mJ with a beam diameter of 5mm were used here. The photolysis beam itself was coaligned along the supersonic flow by sending it through a quartz window

at the Brewster angle at the back of the reactor. The beam exited the reactor through the nozzle throat and a second Brewster angled quartz window attached to the back of the reservoir. As such, C(³P) atoms were generated along the supersonic flow with identical concentrations at any axial position as the UV beam is only weakly attenuated by CBr₄ ($\sigma_{\text{CBr}_4}(266\text{nm}) = 1 \times 10^{-18} \text{ cm}^2$).

C(³P) atoms were detected by pulsed (10 Hz) laser induced fluorescence at vacuum ultraviolet wavelengths (VUV LIF) via the $2s^2 2p^2 \ ^3P_2 \rightarrow 2s^2 2p5d \ ^3D_3^\circ$ transition at 115.803 nm. To generate this wavelength, we first frequency doubled the output of a Nd:YAG pumped dye laser at 695 nm. The residual 695 nm dye laser radiation was then discarded using two dichroic mirrors coated for peak reflectivity at 355 nm so that only the 347 nm UV beam remained. Some of the residual dye laser radiation was fed into the output coupler of a wavemeter to allow us to follow the probe laser wavelength continuously throughout the experiment. The 347 nm beam was directed towards the observation axis of the reactor by right angled quartz prisms where it was focused into a gas cell containing xenon (50 Torr) with argon (160 Torr) added for phase-matching to generate VUV radiation by frequency tripling. H(²S) atoms were also detected during this work, as products of the C + CH₃OCH₃ reaction. This was done using a similar procedure to the one described above for C(³P) atoms to generate a tunable VUV beam around the Lyman- α line at 121.567 nm starting from narrow-band dye laser radiation at 729.4 nm. In this case, krypton (210 Torr) was used as the tripling medium with argon (540 Torr) added for phase-matching. A MgF₂ lens was used as the exit window of the cell to recollimate the VUV beam, leaving the residual UV beam divergent due to the difference in refractive index of MgF₂ at UV and VUV wavelengths. As the cell was attached to the reactor at right angles via a 75 cm long sidearm containing circular baffles, only a low flux of UV radiation reached the observation region. The sidearm was open to the reactor, containing the same residual gases as those present in the reactor including CBr₄ and CH₃OCH₃ which both absorb strongly in the VUV region. As significant attenuation of the VUV probe beam was likely to occur, this region was continuously flushed with either argon or nitrogen during the experiments, thereby preventing residual gases from filling the sidearm. Additional test experiments were performed to check for undesirable effects brought about by the residual UV radiation or the generated VUV radiation. To test for the influence of the residual UV beam entering the reactor, the tripling cell was evacuated to ensure that no C(³P)

and H(²S) signals were observed in the absence of VUV light. To check for the influence of the VUV beam alone, experiments were performed with the photolysis laser off (with gas in the tripling cell) to check for the formation of C(³P) and/or H(²S) by the VUV beam. No signal from C(³P) was ever observed, but a very small H-atom fluorescence signal was observed with CH₃OCH₃ present in the flow, due to CH₃OCH₃ photolysis by the VUV probe beam at 121.567 nm. As this small fluorescence signal represented the same constant contribution for all time points during a single run, this was automatically removed by the baseline subtraction procedure. Resonant emission from the C(³P) or H(²S) atoms in the cold supersonic flow was detected at right angles to both the supersonic flow and the VUV probe laser to minimize scattered light detection from both the photolysis laser and the probe laser. The fluorescence was focused by a lithium fluoride (LiF) lens onto the photocathode of a solar blind photomultiplier tube (PMT – Electron Tubes 9403B). Both the LiF lens and the PMT were isolated from the chamber by a LiF window, thereby avoiding damage to the PMT input window by reactive gases. Atmospheric absorption losses of the VUV fluorescence were eliminated by evacuating the zone containing the LiF lens using a dry vacuum pump. The PMT output signal was processed by a boxcar integration system, while the lasers, boxcar and oscilloscope were synchronized by a digital delay generator operating at 10 Hz. For the present experiments, the C- or H-atom fluorescence signal was measured as a function of delay time between the two lasers. 30 laser shots were recorded and averaged for each time point, with at least 100 points recorded for each temporal trace. 15 of these time points were recorded with the probe laser firing prior to the photolysis laser so unwanted contributions to the signal such as electronic noise, scattered light and the H-atom fluorescence signal generated by CH₃OCH₃ photolysis by the probe laser could be subtracted.

3 Electronic Structure Calculations

The C(³P) + CH₃OCH₃ reaction occurs over the ground state ³A' potential energy surface of C₃H₆O assuming C₁ geometry. The geometries and energies of the reagents/products, intermediates and transition state structures (TSs) were calculated initially using density functional theory (DFT), specifically using the hybrid meta exchange correlation functional, M06-2X,⁴¹ coupled with the aug-cc-pVTZ (AVTZ) basis set (M06-2X/AVTZ). The calculation of harmonic frequencies for these structures allowed us to determine the nature of the stationary point (no imaginary frequencies for a reagent/product species or minimum, a

single imaginary frequency for a TS) and obtain the zero-point energy (ZPE) corrections for all structures. Then, for each identified TS, an intrinsic reaction coordinate calculation was performed to ensure that it lies on the minimum energy pathway between two specified minima. Then, as a second step, we calculated the energies of all species more accurately using domain based local pair-natural orbital singles and doubles coupled cluster theory with an improved perturbative triples correction algorithm (DLPNO-CCSD(T))⁴² as integrated in the ORCA computational package,^{43,44} adopting the geometries derived at the M06-2X/AVTZ level. The DLPNO-CCSD(T) calculations were coupled with the AVTZ basis set here (DLPNO-CCSD(T)/AVTZ). Although all of the underlying calculations were performed with ORCA, the structures were visualized and manipulated using Avogadro,⁴⁵ which was also used to perform the vibrational frequency analysis.

4 Results and discussion

4.1 Potential Energy Surface

The calculated ground state triplet surface ($^3A'$) involved in the $C + CH_3OCH_3$ reaction is shown in Figure 1.

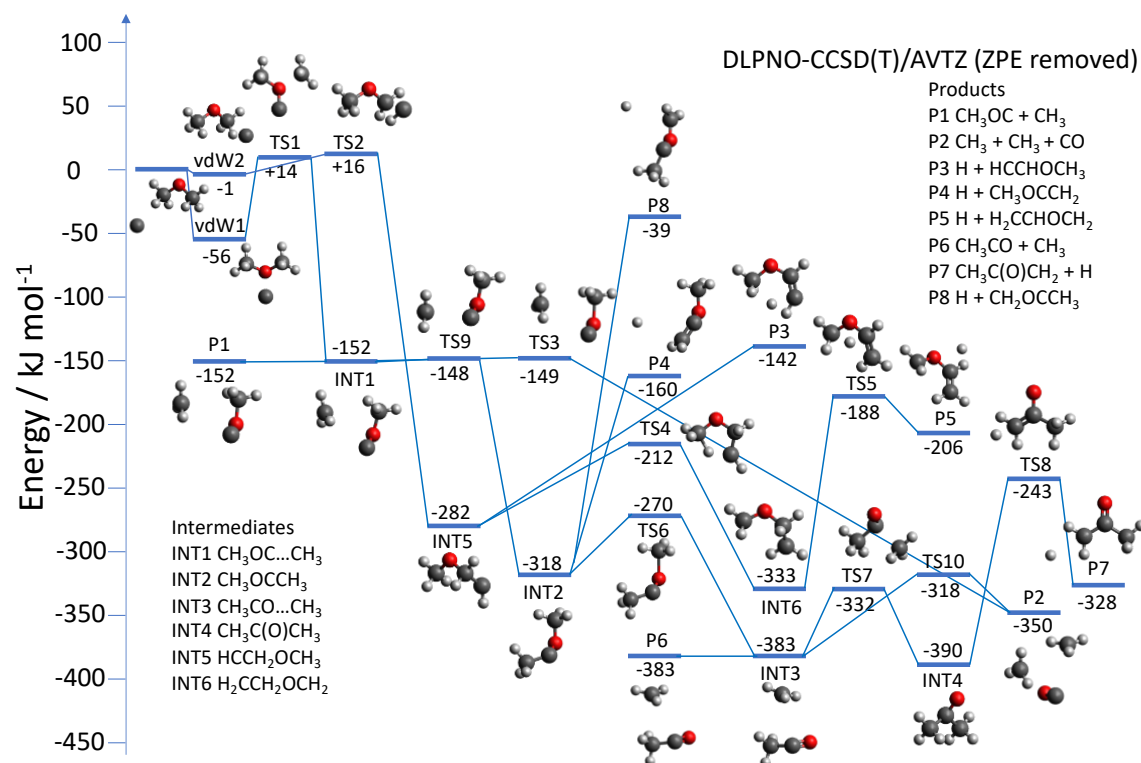


Figure 1 Ground state triplet potential energy surface for the $C(^3P) + CH_3OCH_3$ reaction. All energies are calculated at the DLPNO-CCSD(T)/AVTZ level based on geometries optimized at the M06-2X/AVTZ level. Displayed energies are relative to the reagent $C(^3P) + CH_3OCH_3$ asymptote and are corrected for ZPE differences.

All energies are quoted at the DLPNO-CCSD(T)/AVTZ level relative to the $C + CH_3OCH_3$ entrance channel and are corrected for ZPE differences unless otherwise stated. 8 distinct minima were identified, connected by 10 transition states, leading to 8 different exit channels. The interaction of ground triplet state carbon with CH_3OCH_3 leads to the formation of two possible van der Waals complexes.

Initial carbon attack at the central oxygen atom of CH_3OCH_3 leads to the formation of vdW1 (-56 kJ/mol) with a distance of 1.645 Å between O and the incoming C-atom. vdW1 can then evolve further via TS1 +14 kJ/mol above the reagent level corresponding to the formation of a chemical bond between the incoming C and O followed by breaking of one of the O-CH₃ bonds of CH_3OCH_3 . The resulting weakly bound $CH_3OC...CH_3$ complex (INT1) is calculated to be -152 kJ/mol below the reagent level. Three possible channels are open to INT1. (I) it can dissociate to form $CH_3OC + CH_3$ products (P1) also calculated to be -152 kJ/mol below the reagents. It should be noted here that although the final ZPE corrected DLPNO-CCSD(T) energies are essentially identical, both M06-2X/AVTZ and DLPNO-CCSD(T)/AVTZ calculations indicate that INT1 is more stable than P1 products by -12 and -4 kJ/mol respectively if ZPE differences are not considered. (II) INT1 can isomerize to form the CH_3OCCH_3 intermediate INT2 at -318 kJ/mol, over a very low barrier, TS9, only 4 kJ/mol above INT1. (III) INT1 can dissociate further to products P2, $CH_3 + CH_3 + CO$ (-350 kJ/mol) over another very low barrier, TS3, only 3 kJ/mol above INT1. Of the three possible channels, only INT2 formed by isomerization channel (II) will evolve further. One possibility is that of C-H bond dissociation leading to either $H + CH_2OCCH_3$ products P8, -39 kJ/mol below the reagent level or $H + CH_3OCCH_2$ products (P4), -160 kJ/mol below the reagent level. While scans along the reaction coordinate at the M06-2X/AVTZ level confirmed that the INT2→P4 channel presents no barrier to dissociation, it was not possible to extract any reliable information regarding the INT2→P8 channel at the M06-2X/AVTZ level due to the multiconfigurational nature of this bond dissociation process. Instead, complete active space self-consistent field (CASSCF) calculations using six active orbitals and six active electrons were performed with

the aug-cc-pVDZ basis set, followed by Davidson corrected multireference configuration calculations (MRCI+Q) with the same active space to obtain more accurate energies. These additional calculations were also performed using ORCA.⁴³ During these calculations, the molecule was optimized for each value of the dissociating bond distance between 1 and 4 Å at the CASSCF level while a vibrational frequency analysis was also performed at each step. The energies and vibration frequencies derived in this way were used as inputs in subsequent kinetic calculations described in section 4.2.

Another possibility for evolution of the INT2 intermediate is for the remaining C-O bond of the original CH₃OCH₃ molecule (the H₃C-OCCH₃ bond) to dissociate to form the intermediate CH₃CO...CH₃ species INT3 (-383 kJ/mol) over TS6, 48 kJ/mol above INT2. In a similar manner to INT1 described above, INT3 can (I) dissociate to products P6, CH₃CO + CH₃ (-383 kJ/mol), (II) dissociate further to P2 (-350 kJ/mol) over TS10, 65 kJ/mol above INT3, (III) isomerize to INT4, CH₃C(O)CH₃ (-390 kJ/mol), over TS7, 51 kJ/mol above the INT3 level. INT4 can then lose a hydrogen atom to form products P7, H + CH₃C(O)CH₂ (-328 kJ/mol), by passing over TS8, 147 kJ/mol above INT4.

In an alternative pathway, carbon attack can initially occur at one of the terminal hydrogen atom positions of one of the methyl groups of CH₃OCH₃, leading to the very weakly bound complex vdW2 (-1 kJ/mol) with a newly formed C-H bond distance of 1.500 Å. Given the very low energy of this complex, which is well within the expected theoretical uncertainty of the DLPNO CCSD(T) method (larger than the 4 kJ/mol chemical accuracy of canonical CCSD(T)), this pathway is not considered further in the subsequent kinetic calculations. Nevertheless, for completeness we describe the potential pathways originating from this complex. The weakly bound C-atom can insert into the C-H bond of the methyl group over TS2, +16 kJ/mol above the reagent level, leading to the formation of INT5, HCCH₂OCH₃ (-282 kJ/mol). INT5 can then evolve further by losing a hydrogen atom leading to products P3, H + HCCHOCH₃ (-142 kJ/mol) (only one dissociation pathway is shown here), or by isomerization through H-atom transfer to INT6, H₂CCH₂OCH₂ (-333 kJ/mol). INT6 can dissociate by losing a hydrogen atom through several pathways such as the one over TS5 to form products P5 H + H₂CCHOCH₂ (-206 kJ/mol). Other pathways, such as the abstraction pathway leading to CH + CH₂OCH₃ formation were not considered here as these products are calculated to be endothermic with respect to the C + CH₃OCH₃ entrance channel by +65 kJ/mol at the DLPNO CCSD(T)/AVTZ level.

It should be noted that neither of the two reaction pathways presented here (leading from $C + CH_3OCH_3 \rightarrow vdW1$ or $vdW2 \rightarrow products$) were found to be barrierless at the DLPNO-CCSD(T)/AVTZ//M06-2X/AVTZ level and no other potentially important barrierless reaction channels were identified. Consequently, if we consider the nominal values of the TS1 and TS2 barriers on the ground state PES then the $C + CH_3OCH_3$ reaction is expected to be slow below room temperature in the absence of an important tunneling contribution. The possibility of intersystem crossing to the singlet state, in a similar manner to a recent study of the $O(^3P) + pyridine$ reaction,⁴⁶ was also considered in the present work. MRCI+Q calculations ($2e^-, 4o$) based on CASSCF wavefunctions performed on the $C...O(CH_3)_2$ entrance channel showed that the singlet surface (correlating with $C(^1D) + CH_3OCH_3$ reagents) crosses the triplet surface in the vicinity of TS1, with an energy slightly above the $C(^3P) + CH_3OCH_3$ asymptote. As the CASSCF wavefunctions lead to monoconfigurational wavefunctions, DLPNO-CCSD(T)/AVTZ//M06-2X/AVTZ calculations of the minimum energy crossing point (MECP) should be valid, leading to an energy of +39 kJ/mol for the MECP, even higher than the TS1 and TS2 energies. The geometries and frequencies of all the structures presented in Figure 1 are listed in the supplementary information file.

4.2 Kinetic calculations

According to the electronic structure calculations presented above, the $C + CH_3OCH_3$ reaction is expected to occur through the initial barrierless formation of a complex ($vdW1$, assuming that $vdW2$ is too weakly bound to play any significant role in the reaction) followed by isomerization of this chemically activated species to form the $CH_3OC...CH_3$ (INT1) intermediate. Under these conditions, the predicted overall reaction rate at a specific temperature can be derived from the calculated capture rate constant $k_{capt}(T)$ to form $vdW1$ from the separated reagents, multiplied by the fraction of the population in $vdW1$ that reaches INT1 by passing over TS1. The rate constant calculations reported here were performed using the *Multiwell* suite of programs^{47, 48} in a similar manner to our earlier study of the $C + N_2O$ reaction.⁵ In addition, we have extended the scope of the present work by calculating the product branching fractions at selected temperatures, allowing us to compare directly with the measured H-atom yields.

The initial step was to calculate the energy (E) and angular momentum (J) resolved microcanonical rate constants $k(E, J)$ for the unimolecular dissociation of $vdW1$ to $C +$

CH₃OCH₃ using the *ktools* program⁴⁷ which implements a variational treatment due to the lack of a clearly defined barrier for this process. In order to apply this method, it was necessary to perform a series of constrained optimizations along the reaction coordinate from the equilibrium C..O bond distance of 1.645 Å in vdW1 to the separated reagents. These optimizations were performed at the M06-2X/AVTZ level by increasing the C-O bond distance by 0.2 Å steps along the reaction coordinate until the separation between the carbon and oxygen atom of CH₃OCH₃ reached 6 Å. A subsequent vibrational frequency calculation was then performed at the same level for all of these optimized structures. The harmonic vibrational frequencies orthogonal to the reaction path, the calculated rotational constants and the energies of these structures in addition to those of the separated reagents and vdW1 complex (all calculated at the DLPNO-CCSD(T)/AVTZ level) served as inputs for the *ktools* calculations⁴⁷ which were performed using a small grain size of 1 cm⁻¹ for better accuracy at low temperature. The calculated frequencies and energies are listed in Table S4. Trial rate constants were calculated for each fixed distance, with the variational transition state given by the point yielding the minimum trial rate constant value. When multiple significant minima were located, as was the case for the entrance channel leading to vdW1, a multiple transition state model was applied based on the unified statistical theory of Miller.⁴⁹

Averaging the values of $k(E, J)$ over E and J at a given temperature,⁵⁰ allowed us to calculate the canonical rate constants, equivalent to the high-pressure-limit rate constant, $k_{\infty}^{uni}(T)$. The capture rate constant, $k_{capt}(T)$, was then determined from the equilibrium constant, $K_{eq}(T)$, through expression (1)

$$k_{capt}(T) = k_{\infty}^{uni}(T)/K_{eq}(T) \quad (1)$$

The values of $k_{capt}(T)$ derived in this way for a range of temperatures between 50 and 296 K were used as inputs for subsequent master equation (ME) simulations to obtain the final overall temperature and pressure-dependent rate constants and product branching ratios. RRKM statistical theory as implemented in *Multiwell*⁴⁷ was employed to derive energy-dependent microcanonical rate constants $k(E)$ for a specific reaction step

$$k(E) = L^{\ddagger} \frac{g_e^{\ddagger}}{g_e} \frac{1}{h} \frac{G^{\ddagger}(E-E_0)}{\rho(E)} \quad (2)$$

where $L^{\ddagger} = \frac{m^{\ddagger}}{m} \times \frac{\sigma_{ext}}{\sigma_{ext}^{\ddagger}}$ is the reaction path degeneracy, with m^{\ddagger} and m the number of optical isomers of the TS and reagent respectively, σ_{ext}^{\ddagger} and σ_{ext} are the external rotation symmetry numbers, for the TS and reagent respectively. g_e^{\ddagger} and g_e are the electronic state degeneracies

of the transition state and reactant, respectively. h is Planck's constant, $G^\ddagger(E - E_0)$ is the sum of states for the TS, E_0 is the reaction threshold energy and $\rho(E)$ is the reagent molecule state density.

The ME simulations were initiated from the chemically activated complex well, vdW1*. This species can evolve initially through three different pathways. (I) it can redissociate to reagents C + CH₃OCH₃; (II) it can surmount the barrier TS1 to form INT1; (III) it can stabilize to vdW1 through collisions with the carrier gas. Preliminary calculations showed that stabilization of the chemically activated complex was negligible over the range of pressures and temperatures used in the experiments, so pathway (III) is not expected to play a role in the current experiments. If pathway (II) is followed, INT1 is allowed to evolve further in the present simulations as the various other possible wells (INT2, INT3 and INT4), TSs (TS3, TS6, TS7, TS8, TS9, TS10) and product channels connected to vdW1 are also taken into consideration. The total rate constant $k(T, [M])$ is determined by expression (3)

$$k(T, [M]) = k_{capt}(T) \left(1 - f_{C+CH_3OCH_3}(T, [M]) \right) \quad (3)$$

where $f_{C+CH_3OCH_3}(T, [M])$ is the fraction of vdW1* molecules that redissociate to reagent molecules at the end of the simulation, following pathway (I). In order to derive the branching fractions of the various individual product channels, the following expression was applied

$$f_P(T, [M]) / \left(1 - f_{C+CH_3OCH_3}(T, [M]) \right) \quad (4)$$

where $f_P(T, [M])$ is the fraction of product molecules in channel P formed at the end of the simulation.

The simulations were performed over a wide range of pressures (100 kPa - 1×10^{-8} Pa) and over the experimental temperature range (50-296 K), to check for possible pressure dependent effects in the experiments. Here, a grain size of 1 cm^{-1} was used to obtain better precision at low temperature and to be consistent with the results of the *ktools* calculations described above. Lennard-Jones parameters for the carrier gases Ar and N₂ were taken from the literature⁵¹ while they were estimated for the well species INT1, INT2, INT3, and INT4 ($\sigma = 5.0 \text{ \AA}$, $\varepsilon / k_B = 300 \text{ K}$). The standard exponential-down model⁵² was used to describe energy transfer.

Sums and densities of states for wells vdW1, INT1, INT2, INT3, and INT4 as well as transition states TS1, TS3, TS6, TS7, TS8, TS9 and TS10 were calculated by the *Densum* program.⁴⁷ As *Densum* is only suitable for obtaining these quantities from fixed TSs, the barrierless entrance

channel and the dissociation channels INT1→P1, INT2→P8 and INT3→P6 were all treated with the *ktools* program (here, the energies and vibrational frequencies for the INT→P8 channel used in the *ktools* calculations were derived at the MRCI+Q/AVDZ level employing CASSCF wavefunctions as described in section 4.1), allowing us to obtain the sums and densities of states for these pathways. Reaction enthalpies ($\Delta H_{\text{rxn}}(0 \text{ K})$) were supplied by single point calculations at the DLPNO-CCSD(T)/AVTZ level, in addition to the zero-point corrected reaction critical energies (barrier heights with ZPE correction) where the ZPEs of the various species were derived from DFT calculations at the M06-2X/AVTZ level.

4.3 Rate constants

Several representative plots of the variation of the C(³P) VUV LIF signal as a function of time recorded at 127 K are displayed in Figure 2.

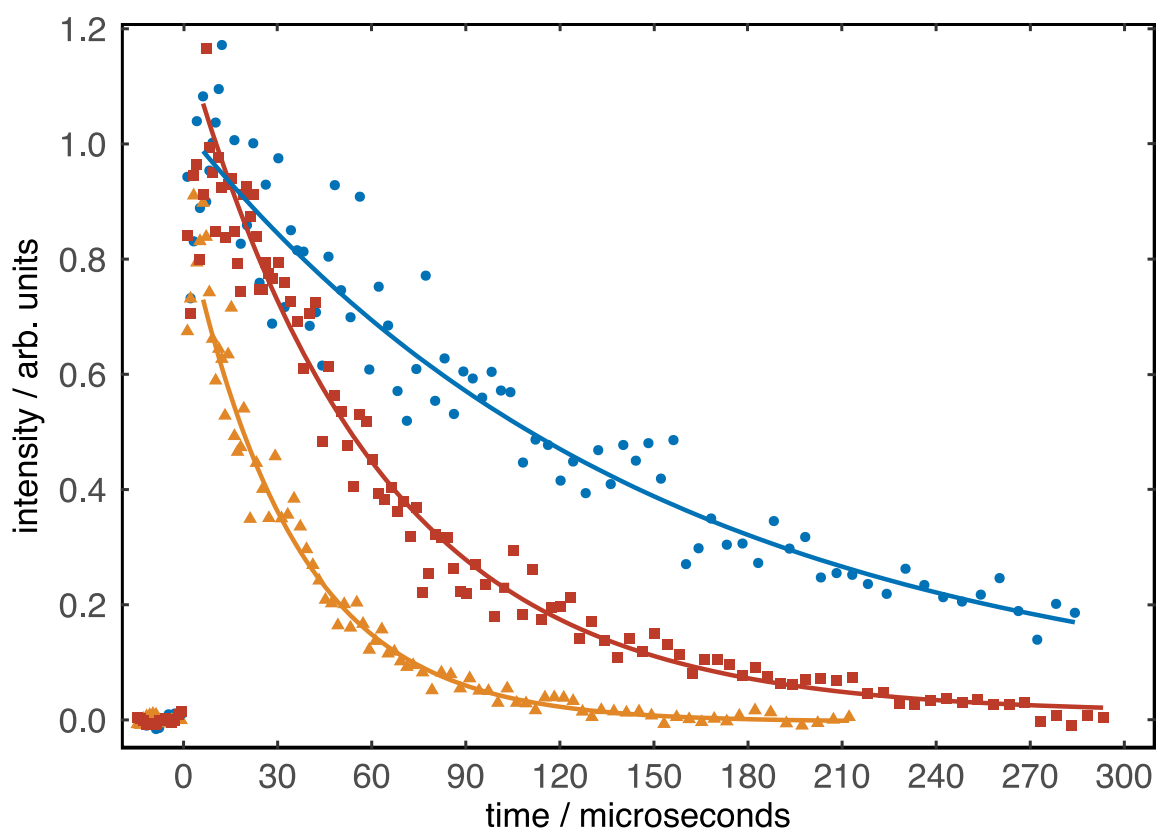


Figure 2 C(³P) VUV LIF signal plotted as a function of delay time recorded at 127 K. (Blue circles) $[\text{CH}_3\text{OCH}_3] = 0 \text{ cm}^{-3}$; (red squares) $[\text{CH}_3\text{OCH}_3] = 2.0 \times 10^{14} \text{ cm}^{-3}$; (orange triangles) $[\text{CH}_3\text{OCH}_3] = 6.0 \times 10^{14} \text{ cm}^{-3}$. The solid lines show the derived exponential fits to the individual datasets based on expression (5).

As CH₃OCH₃ concentrations were always much greater than the C(³P) atom concentration, the kinetic data could be analyzed assuming that the CH₃OCH₃ concentration did not change during the course of the reaction. In this respect, C(³P) atoms were considered to decay according to a first-order rate law (the so called pseudo-first-order approximation), obeying the following expression

$$I(t) = I_0 \exp(-k_{1st}t) \quad (5)$$

$I(t)$ and I_0 are the time dependent and initial C(³P) VUV LIF intensities respectively (arbitrary units), k_{1st} is the pseudo-first-order decay constant for C(³P) loss (s⁻¹) and t is the delay time (s). The temporal dependence of the C(³P) fluorescence signal is well described by expression (5), decaying exponentially even in the absence of coreagent CH₃OCH₃. This occurs due additional reactive losses of C(³P) atoms such as through their reaction with CBr₄ molecules ($k_{C+CBr_4}[CBr_4]$) or impurities in the carrier gas ($k_{C+X}[X]$), in addition to their diffusive losses (diffusion out of the zone illuminated by the probe laser, k_{diff}). These three terms are constant for any single series of measurements, so the change in decay constant shown in figure 3 is due to the varying term $k_{C+CH_3OCH_3}[CH_3OCH_3]$ where $k_{C+CH_3OCH_3}$ is the second-order rate constant for the C(³P) + CH₃OCH₃ reaction. Consequently, $k_{C+CH_3OCH_3}$ can be determined at a given temperature by plotting the derived k_{1st} values as a function of the corresponding CH₃OCH₃ concentration as shown in Figure 3.

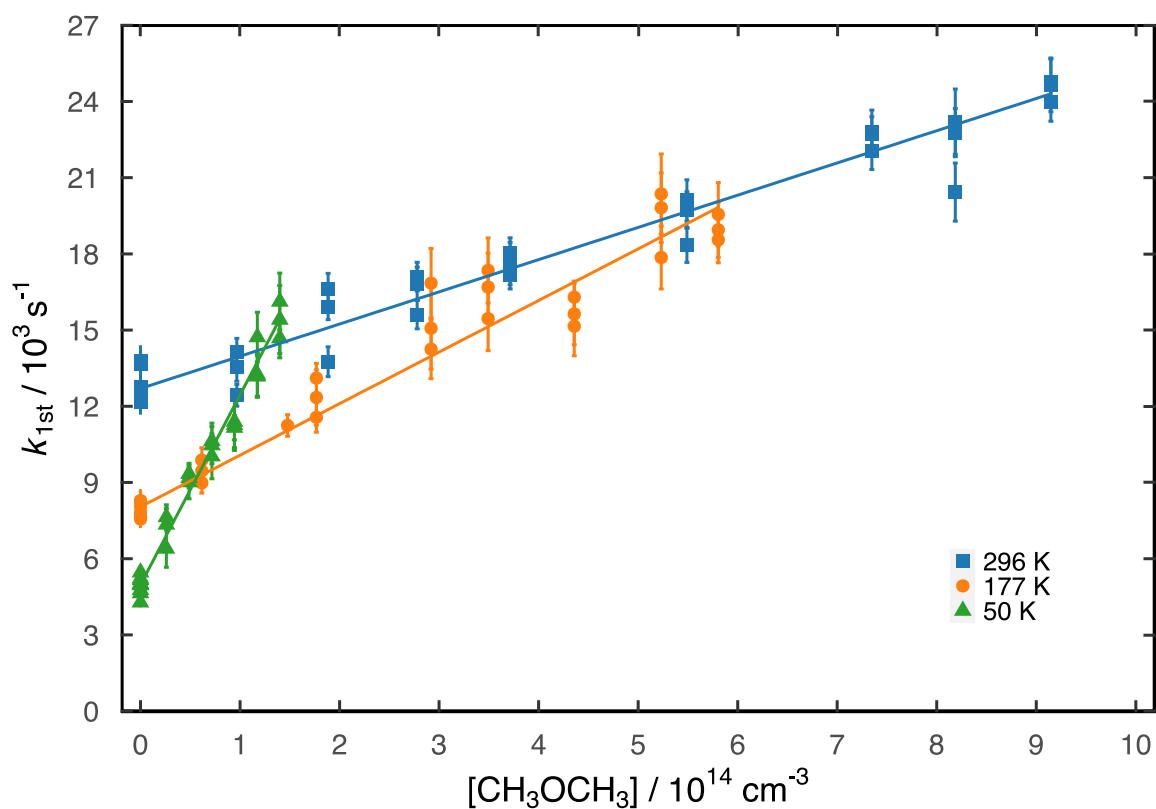


Figure 3 Derived pseudo-first-order rate constants as a function of the CH₃OCH₃ concentration for experiments performed at various temperatures. (Blue solid squares) data recorded at 296 K; (orange solid circles) data recorded at 177 K; (green solid triangles) data recorded at 50 K. Solid lines represent weighted linear least-squares fits to the individual datasets yielding the second-order rate constants, $k_{C+CH_3OCH_3}$, from the slopes.

The derived second-order rate constants are plotted as a function of temperature in Figure 4 and are summarized in Table 1 alongside other relevant information.

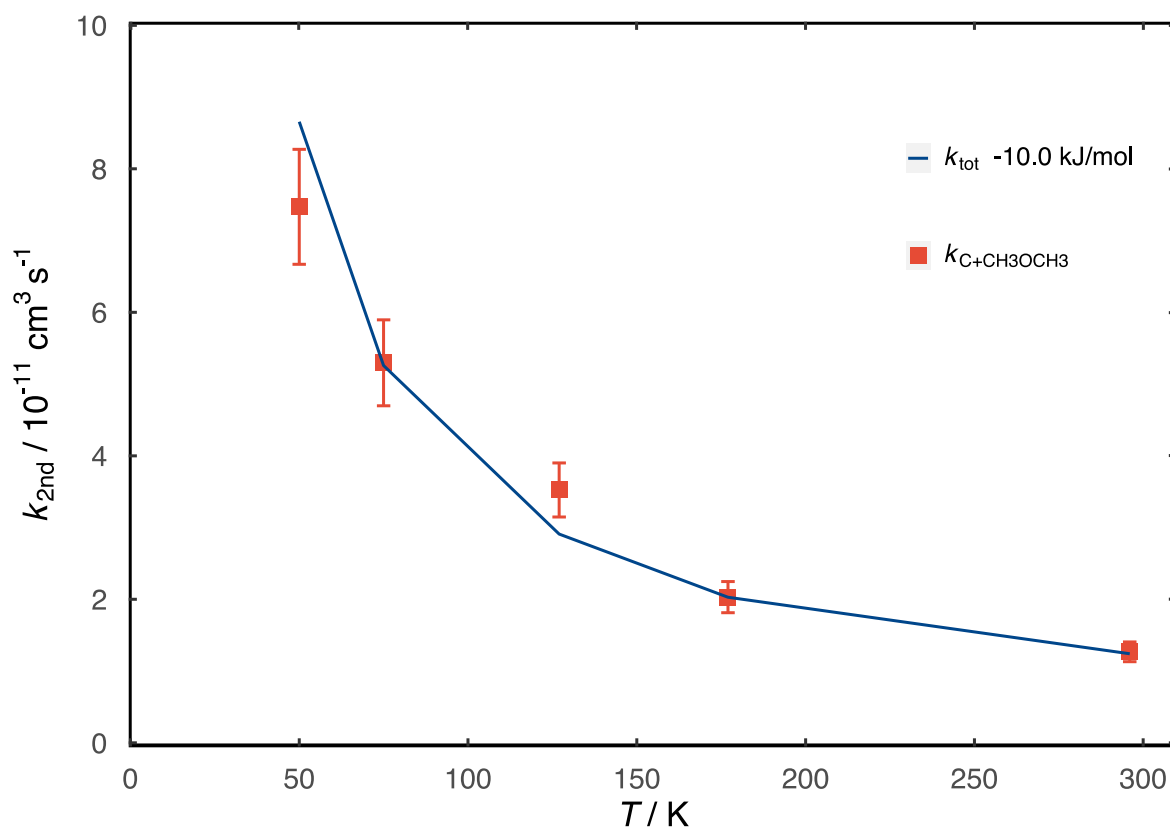


Figure 4 Temperature dependence of the second-order rate constants for the $\text{C}(^3\text{P}) + \text{CH}_3\text{OCH}_3$ reaction. (Red solid squares) this experimental work. Error bars represent the combined statistical (single standard deviation) and estimated systematic errors (10 %) of the nominal rate constant value. (Solid blue line) second-order rate constants calculated by the ME simulations assuming a submerged barrier of -10 kJ/mol for TS1.

Table 1 Second-order rate constants for the $\text{C}(^3\text{P}) + \text{CH}_3\text{OCH}_3$ reaction

T / K	N^b	Carrier gas	$[\text{CH}_3\text{OCH}_3]$ / 10^{13} cm^{-3}	Flow density / 10^{17} cm^{-3}	$k_{\text{C}(^3\text{P})+\text{CH}_3\text{OCH}_3}^{\square}$ / $10^{-11} \text{ cm}^3 \text{ s}^{-1}$	$k_{\text{C}(^3\text{P})+\text{CH}_3\text{OCH}_3}^{\square}$ / $10^{-11} \text{ cm}^3 \text{ s}^{-1}$
296	30	Ar	0 - 91.5	1.64	$(1.27 \pm 0.14)^c$	1.24 ^d
177 ± 2 ^a	28	N ₂	0 - 58.1	0.94	(2.03 ± 0.22)	2.03
127 ± 2	30	Ar	0 - 66.0	1.26	(3.52 ± 0.38)	2.91
75 ± 2	21	Ar	0 - 18.9	1.47	(5.30 ± 0.60)	5.26

50 ± 1	27	Ar	0 - 14.0	2.59	(7.47 ± 0.80)	8.66
--------	----	----	----------	------	---------------	------

^aThe uncertainties attributed to the calculated temperatures represent the statistical (1σ) errors obtained from the variations of the impact pressure as a function of distance obtained by Pitot tube measurements. ^bNumber of individual measurements. ^cMeasured rate constants. Uncertainties represent the combined statistical (1σ) and estimated systematic errors (10%). ^dCalculated rate constants obtained by adopting a value of -10.0 kJ/mol for TS1.

The C + CH₃OCH₃ reaction is seen to display a significant negative temperature dependence over the 50-296 K range with rate constants increasing by more than a factor of five from $(1.3 \pm 0.1) \times 10^{-11} \text{ cm}^3 \text{ s}^{-1}$ at 296 K to $(7.5 \pm 0.8) \times 10^{-11} \text{ cm}^3 \text{ s}^{-1}$ at 50 K. A simple fit to these data of the form $k(T) = \alpha(T/300)^\beta$ can be used to represent the rate constants for this reaction that are appropriate for use in astrochemical models with $\alpha = (1.27 \pm 0.40) \times 10^{-11}$ and $\beta = -1.01 \pm 0.07$. If we extrapolate the fit down to a typical dense interstellar cloud temperature of 10 K, a value of $k_{\text{C+CH}_3\text{OCH}_3}(10 \text{ K}) = 4.01 \times 10^{-10} \text{ cm}^3 \text{ s}^{-1}$ is obtained. While qualitatively similar temperature dependences were observed in earlier studies of the related C + CH₃OH⁵³ and C + NH₃ reactions,³⁶ the reactions of atomic carbon with acetonitrile, CH₃CN,⁵⁴ and acetone, CH₃COCH₃⁵⁵ display contrasting behaviour, being rapid over the entire temperature range between 50 and 296 K, with little or no temperature dependence. This difference appears to be due the nature of the TS separating the initial complex formed by the reagents from the more stable adducts over the respective potential energy surfaces. Indeed, while the C + CH₃OH and C + NH₃ reactions are characterized by TSs that are close in energy to the reagent level, the C + CH₃CN and C + CH₃COCH₃ reactions display TSs that are much lower in energy. As a result, once the initial complex is formed during the reactions of C with CH₃OH and NH₃, it is equally likely to redissociate to reagents at higher temperature as it is to pass through to products. At low temperature, the forward process dominates due to the lower barrier for product formation. Although the C + CH₃OCH₃ reaction behaves in a similar manner to the C + CH₃OH and C + NH₃ reactions, indicating the possible presence of a submerged TS, the results of the electronic structure calculations described in section 4.1 predict a real barrier to product formation in this case.

As a first attempt to simulate the experimental results through the kinetic calculations described in section 4.2, we used the nominal value of the TS1 activation barrier of + 14 kJ/mol obtained at the DLPNO-CCSD(T)/AVTZ//M06-2X/AVTZ level in test ME simulations performed at 296 K and at 50 K, in the absence of tunneling effects. Unsurprisingly, given the relatively

high positive value of this TS, large values of $f_{C+CH_3OCH_3}(T, [M])$ were calculated at both temperatures, corresponding to more than 99.9 % of the initial vdW1* population redissociating to reagents C + CH₃OCH₃. When tunneling was included for these calculations, through the use of an unsymmetrical Eckart barrier, the results were the same as those performed in the absence of tunneling. At 296 K, the resulting total rate constant, $k(T, [M])$, was calculated to be several orders of magnitude lower than the measured value of $(1.3 \pm 0.1) \times 10^{-11} \text{ cm}^3 \text{ s}^{-1}$ at this temperature. As stabilization of vdW1 was already shown to be negligible at all temperatures for the pressures used in the present experiments, only a significant flux over TS1 can explain the magnitude of the measured rate constants. Consequently, the energy of TS1 was adjusted until good agreement with the experimental rate constants was obtained, while all other parameters including the vdW1 well depth were kept at their original values. The best agreement between theory and the experimental results over the 50-296 K range as shown in Figure 4 and summarized in Table 1 was obtained for a TS1 value of -10 kJ/mol, 24 kJ/mol lower than the value derived from the electronic structure calculations. In order to evaluate whether such a large change in the energy of TS1 is reasonable, we performed additional calculations of the ZPE corrected TS1 energy (relative to the C+ CH₃OCH₃ level) with a variety of methods. The results of these additional calculations are shown in Table 2.

Table 2 Calculated TS1 energies corrected for ZPE effects relative to the C + CH₃OCH₃ reagent level.

Method	TS1 energy / kJ mol ⁻¹
M06-2X/AVTZ	-8.8
M06-2X/AVQZ ^a	-9.7
M06-2X/CBS ^b	-6.3
B3LYP/AVTZ	-21.0
B2PLYP-D3/AVTZ	-12.2
DLPNO-CCSD(T)/AVTZ//M06-2X/AVTZ ^c	+14.2
DLPNO-CCSD(T)/CBS//M06-2X/CBS	+10.2
CCSD(T)/AVTZ//M06-2X/AVTZ	+9.6

DLPNO-CCSD(T)/AVTZ//B3LYP/AVTZ	+14.4
CCSD(T)/AVTZ//B3LYP/AVTZ	+8.3
DLPNO-CCSD(T)/AVTZ//B2PLYP-D3/AVTZ	+14.4

^a aug-cc-pVQZ basis set. ^b Extrapolation to the complete basis set limit. ^cThis method was used to obtain the energies displayed in Figure 1.

It can be seen that the DFT based methods in general lead to negative values of the TS1 energy including the M06-2X/CBS calculations where the results of calculations performed with M06-2X functional employing the AVTZ and AVQZ basis sets are extrapolated to the complete basis set limit. In contrast, the results of the coupled cluster based methods employing molecular geometries obtained at the DFT level all predict a positive value for the TS1 energy with the canonical CCSD(T) calculations leading to smaller barrier heights by a few kJ/mol than the more approximate DLPNO-CCSD(T) ones.

4.4 Product Branching Ratios

To obtain quantitative information regarding the product branching ratios of the $C(^3P) + CH_3OCH_3$ reaction, separate experiments were performed to measure the product H-atom VUV LIF signal intensities as a function of reaction time. These relative intensities were then compared with those obtained from a reference process, the $C(^3P) + C_2H_4$ reaction with a known H-atom yield of 0.92 ± 0.04 at 300 K,⁵⁶ allowing us to derive absolute H-atom product yields. Previous studies⁵⁷ have shown that the H-atom yield of the $C(^3P) + C_2H_4$ reaction should not change significantly at the temperatures and pressures used in the present work. As $C(^1D)$ atoms are also generated during the photolysis of CBr_4 molecules at 266 nm, it was necessary to consider the possibility of H-atom production by the $C(^1D) + C_2H_4$ and $C(^1D) + CH_3OCH_3$ reactions. To lower the concentration of $C(^1D)$ atoms in the supersonic flow, N_2 was used as the carrier gas in experiments conducted at 296 K, while N_2 is already used as the carrier gas at 177 K. For the experiments performed at 75 K, where Ar is the carrier gas, a large concentration of N_2 ($1.5 \times 10^{16} \text{ cm}^{-3}$) was added to the flow. The results of earlier experiments to characterize the flow properties when adding large N_2 concentrations indicated a slight increase in the flow temperature of a few Kelvin.⁵⁸ The $C(^1D) + N_2 \rightarrow C(^3P) + N_2$ quenching reaction becomes more efficient as the temperature falls with measured rate constants of

$(5.3 \pm 0.5) \times 10^{-12} \text{ cm}^3 \text{ s}^{-1}$ at 296 K increasing to $(10.7 \pm 1.1) \times 10^{-12} \text{ cm}^3 \text{ s}^{-1}$ at 75 K.³⁵ Consequently, any $\text{C}(^1\text{D})$ atoms present in the flows are expected to be removed under our experimental conditions within the first few microseconds at all temperatures. Typical H-atom formation curves recorded for the $\text{C} + \text{CH}_3\text{OCH}_3$ (blue points) and $\text{C} + \text{C}_2\text{H}_4$ (red points) reactions are shown in Figure 5.

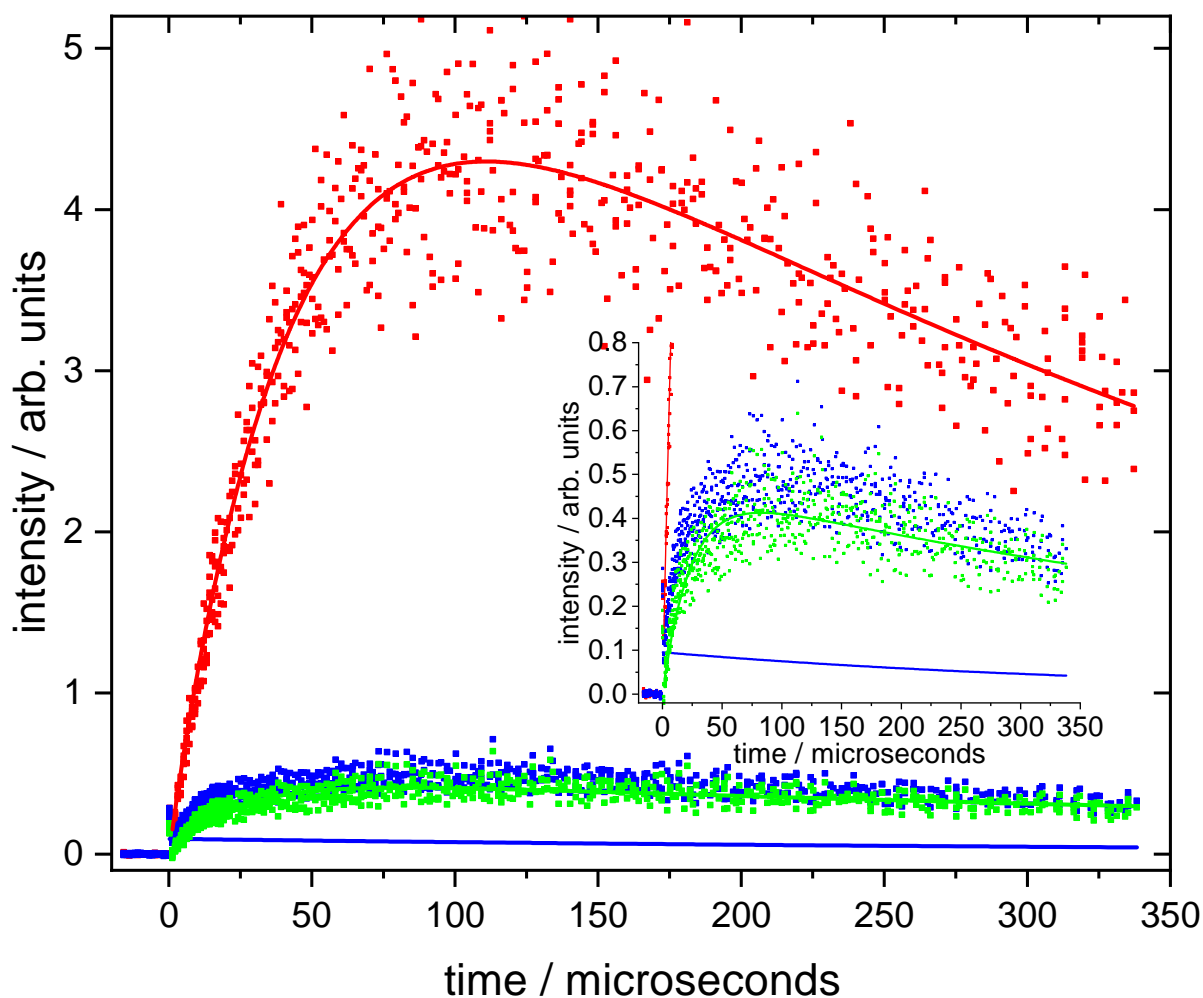


Figure 5 H-atom VUV LIF signal intensity as a function of reaction time for the $\text{C} + \text{CH}_3\text{OCH}_3$ and $\text{C} + \text{C}_2\text{H}_4$ reactions recorded at 75 K. (Dark blue squares) H-atom signal from the reaction of both $\text{C}(^3\text{P})$ and $\text{C}(^1\text{D})$ with CH_3OCH_3 where $[\text{CH}_3\text{OCH}_3] = 9.8 \times 10^{13} \text{ cm}^{-3}$. (Red solid squares) The $\text{C} + \text{C}_2\text{H}_4$ reaction with $[\text{C}_2\text{H}_4] = 1.5 \times 10^{13} \text{ cm}^{-3}$. (Solid green squares) H-atom signal attributed to the $\text{C}(^3\text{P}) + \text{CH}_3\text{OCH}_3$ reaction alone following subtraction of the instantaneous H-atom signal arising from the $\text{C}(^1\text{D}) + \text{CH}_3\text{OCH}_3$ reaction. (Solid blue line) Estimated H-atom signal arising from the $\text{C}(^1\text{D}) + \text{CH}_3\text{OCH}_3$ reaction. Solid red and green lines represent non-linear fits to the individual datasets using expression (6).

The curves plotted in Figure 5 are the result of several different experiments for both reactions, recorded alternately, which have then been coadded. While the H-atom formation curve for the $C + C_2H_4$ reaction shows a H-atom signal close to zero at short delay times, for the $C + CH_3OCH_3$ reaction it can be seen that there is an abrupt increase in the H-atom signal at short times followed by a slower rise at longer times. This rapid rise is likely to be due to the presence of unquenched $C(^1D)$ atoms present in the flow for the first few microseconds which then react with CH_3OCH_3 leading to a quasi-instantaneous production of atomic hydrogen which contributes to the overall H-atom signal. Similar contributions are also observed for those experiments performed at 177 and 296 K where N_2 was used as the carrier gas. This observation allows us to make certain hypotheses regarding the $C(^1D) + CH_3OCH_3$ reaction. Firstly, it is likely that the rate constants for the $C(^1D) + CH_3OCH_3$ reaction are considerably larger than those of the $C(^3P) + CH_3OCH_3$ reaction, in a similar manner to the $C(^3P/^1D) + CH_3OH$ reactions where the $C(^1D) + CH_3OH$ reaction was measured to be ten times faster than the corresponding $C(^3P) + CH_3OH$ reaction at 296 K with little or no temperature dependence.⁵³ Secondly, given the magnitude of the instantaneous signal, it could be that the H-atom yield of the $C(^1D) + CH_3OCH_3$ reaction is much larger than the one we measure for the $C(^3P) + CH_3OCH_3$ reaction. This conclusion was also reached during our earlier studies of the $C(^1D) + CH_4$, C_2H_6 reactions⁵⁹ and during our study of the closely related $C(^1D) + CH_3OH$ reaction⁵³ where H-atom yields were all close to unity. Despite the use of N_2 as the carrier gas, the instantaneous signal is larger at higher temperature due to the smaller rate constants of the $C(^3P) + CH_3OCH_3$ reaction as the temperature increases. Indeed, the fact that the reaction rate is lower at higher temperature also means that larger CH_3OCH_3 concentrations are required to measure kinetic decays over similar timescales, while the difference in rate constants between the two processes is likely to be the greatest at higher temperature.

A similar issue is not expected to arise for the $C(^3P/^1D) + C_2H_4$ reactions for several reasons. Firstly, the $C(^3P) + C_2H_4$ is already very fast, with rate constants greater than $3 \times 10^{10} \text{ cm}^3 \text{ s}^{-1}$ at room temperature and below with only a weak temperature dependence,⁹ meaning that lower concentrations of C_2H_4 are typically used for these experiments, reducing the contribution of the $C(^1D) + C_2H_4$ reaction to the overall H-atom signal. Consequently, as the $C(^1D) + C_2H_4$ reaction occurs on a much longer timescale, it is likely that most of the $C(^1D)$ atoms present in the flow following photolysis are already quenched to the ground state

through collisions with the carrier gas before significant production of H-atoms occurs. Secondly, the H-atom yield of the $C(^3P) + C_2H_4$ reaction is already close to unity, in contrast to the $C(^3P) + CH_3OCH_3$ reaction, so that this signal almost certainly overwhelms the one from the $C(^1D) + C_2H_4$ reaction.

As the H-atom signal contribution from the $C(^1D) + CH_3OCH_3$ reaction occurs instantaneously, it can be subtracted from the overall signal relatively easily by estimating the H-atom signal at short delay times. As these H-atoms are expected to be lost mostly by diffusion from the observation region, this instantaneously produced H-atom signal is expected to decay exponentially as a function of time. The $H + CH_3OCH_3$ association reaction is not expected to play a role in H-atom loss due to the presence of an activation barrier for this process. An estimation of the decay time constant was made by examining the time constants of similar H-atom decay profiles obtained in earlier experiments under similar conditions. The final contribution to be subtracted from the H-atom production curves of the $C + CH_3OCH_3$ reaction for experiments performed at 75 K is shown as a solid blue line in Figure 5. The resulting subtraction shown as green squares is well described by the following biexponential function

$$I_H = A\{exp(-k_{L(H)}t) - exp(-k_{1st}t)\} \quad (6)$$

where I_H is H-atom fluorescence signal, $k_{L(H)}$ is the secondary H-atom loss term which occurs through processes such as diffusion with k_{1st} equal to the first-order formation rate of atomic hydrogen. A is the predicted amplitude in the absence of H-atom losses (when $k_{L(H)} = 0$, $exp(-k_{L(H)}t) = 1$). The derived biexponential fit using expression (6) is shown as a solid green line in Figure 5. As small variations in the derived fitting parameters led to significant variations in predicted A value in the present analysis, we chose instead to compare the peak values given by the biexponential fits to the data. The peak intensities of the H-atom formation curves for the $C + C_2H_4$ reference reaction were divided by 0.92 to correct for the fact that the measured H-atom yields for this process are smaller than 1.⁵⁶ The peak intensities of the H-atom formation curves for the $C + CH_3OCH_3$ reaction were also corrected for VUV absorption losses in the present experiments as the high CH_3OCH_3 concentrations used here were estimated to result in absorption losses at 121.567 nm as high as 25 % in the worst case (experiments conducted at 296 K). The derived absolute H-atom yields for the $C(^3P) + CH_3OCH_3$ reaction are listed in Table 3 alongside the product branching ratios predicted by

the ME analysis described in section 4.2, using the same TS1 energy of -10 kJ/mol as used in the kinetic simulations. As mentioned earlier, the pathways originating from vdW2 are not considered due the very small predicted well depth which is well within the expected error bars of the calculations. No other energies were modified during the present calculations.

Hydrogen atoms and their accompanying molecular coproducts are clearly only minor products of the C + CH₃OCH₃ reaction considering the very low H-atom yield when compared with the H-atom yield of the C + C₂H₄ → C₃H₃ + H reaction shown in red in Figure 5.

Table 3 Measured and calculated branching ratios (%) of the various reaction channels for the C(³P) + CH₃OCH₃ reaction. (The experimental measurement (Expt.) represents the sum of all H-atom production channels, which should be compared to the sum of P4 and P8.)

T / K	P2	P1	P6	P8	P4	P8+P4	Expt.
50	67.4	28.8	0.1	1.7	2.1	3.8	
75 ± 2 ^a	67.3	28.9	0.1	1.7	2.1	3.8	8.9
127	67.6	28.6	0.1	1.7	2.0	3.7	
177 ± 2	67.9	28.3	0.1	1.7	2.0	3.7	7.8±5.3 ^b
296	68.5	27.7	0.1	1.7	2.0	3.7	9.9±4.9

^aThe uncertainties attributed to the calculated temperatures represent the statistical (1σ) errors obtained from the variations of the impact pressure as a function of distance obtained by Pitot tube measurements. ^bErrors represent the 95% confidence level (no error is cited for the measurement performed at 75 K as this is the result of a single series of coadded measurements).

Table 3 lists only those product channels with a non-zero yield predicted by the ME calculations (the yield for products P7, H + CH₃COCH₂, for example was always zero in the present simulations, while the yields for products P3 and P5 were also zero because the pathways from vdW2 were not considered). The principal result of these simulations is that pathways leading to products of lower molecular complexity dominate for the C + CH₃OCH₃ reaction. It can be seen that pathway INT1→TS3→P2 leading to the formation of CH₃ + CH₃ + CO is the major channel, representing approximately 67-68 % of the total according to our calculations, with little predicted variation as a function of temperature. The pathway INT1→P1 leading to the formation of CH₃OC + CH₃ is also important (28-29%) although it is probable that a significant fraction of the CH₃OC formed here will dissociate further to CH₃ +

CO. The INT1→TS9→INT2→TS6→INT3→P6 channel leading to the formation of CH₃ + CH₃CO is predicted to be essentially negligible, representing only 0.1 % of the calculated overall product yield. Although the major outcome of this reaction appears to be the formation of less complex products, there are two other minor channels INT1→TS9→INT2→P4 (H + CH₃OCCH₂) and INT1→TS9→INT2→P8 (H + CH₂OCCH₃) predicted by the ME calculations that lead to an increase in molecular complexity and the elimination of an H-atom. As the experiments measure the sum of all H-atom production channels, the measured H-atom yields should be compared to the sum of the calculated H-atom yields P4 and P8 as shown in Table 3. In order to correctly account for these C-H bond dissociation channels, where three C-H bonds can dissociate for each of the two CH₃ groups, we included three equivalent bond dissociation pathways in the ME calculations for both INT2→P4 and INT2→P8. Additional constrained optimizations from the CH₃OCCH₃ intermediate at the M06-2X/AVTZ level, performed by increasing the C-H distance from its equilibrium value to the separated products P4 for an alternative C-H bond showed that these pathways are effectively equivalent. These channels are calculated to represent approximately 4 % (this falls to 3 % if only one C-H dissociation channel is included for each CH₃ group) of the overall product yield of this reaction, in reasonable agreement with the low measured H-atom yields. In this respect, the experiments and calculations show good qualitative agreement by predicting that the channels leading to an increase in molecular complexity (those accompanied by the production of H-atoms) are clearly only a minor product of the C + CH₃OCH₃ reaction, while this reaction could be a source of CH₃ and CO in the interstellar medium.

5 Astrophysical Implications

Current astrochemical models largely underestimate the abundance of CH₃OCH₃ in dense clouds,⁶⁰ even before the introduction of the C + CH₃OCH₃ reaction. Here, we test the effects induced by including this reaction in a standard astrochemical model, the Nautilus code⁶¹ (a 3-phase gas, dust grain ice surface and dust grain ice mantle time dependent chemical model employing kida.uva.2014²⁹ as the basic reaction network) updated recently for a better description of COM chemistry on interstellar dust grains and in the gas-phase.^{62, 63} There are 800 individual species included in the network that are involved in approximately 9000 separate reactions. Elements are either initially in their atomic or ionic forms in this model

(elements with an ionization potential < 13.6 eV are considered to be fully ionized) and the C/O elemental ratio is equal to 0.71 in this work. The initial simulation parameters are listed in Table 4.

Table 4 Elemental abundances and other model parameters

Element	Abundance ^(a)	$n\text{H} + 2n\text{H}_2 / \text{cm}^{-3}$	T/ K	Cosmic ray ionization rate / s^{-1}	Visual extinction
H ₂	0.5	2.5×10^4	10	1.3×10^{-17}	10
He	0.09				
C ⁺	1.7×10^{-4}				
N	6.2×10^{-5}				
O	2.4×10^{-4}				
S ⁺	6.0×10^{-7}				
Fe ⁺	2.0×10^{-8}				
Cl ⁺	1.0×10^{-7}				
F	6.7×10^{-9}				

^(a)Relative to total hydrogen ($n\text{H} + 2n\text{H}_2$)

The grain surface and the mantle are both chemically active for these simulations, while accretion and desorption are only allowed between the surface and the gas-phase. The dust-to-gas ratio (in terms of mass) is 0.01. A sticking probability of 1 is assumed for all neutral species while desorption occurs by both thermal and non-thermal processes (cosmic rays, chemical desorption) including sputtering of ices by cosmic-ray collisions.⁶⁴ The formalism used to describe the surface reactions and a more detailed description of the simulations can be found in Ruaud et al.⁶¹

The reactions involved in CH₃OCH₃ production and destruction are shown in Table S5 of the supplementary information file. In our updated network, four reactions lead to CH₃OCH₃ formation. First, there is the radiative association reaction between CH₃ and CH₃O.⁶⁰ Second, the electronic dissociative recombination of CH₃OHCH₃⁺ also leads to CH₃OCH₃ production.⁶⁵⁻
⁶⁷ Two other reactions take place on the grains, firstly the s-CH₃ + s- CH₃O reaction (s- means species on the grain) and finally the C + s- CH₃OH reaction followed by hydrogenation of s-

CH₃OCH₃. To estimate the efficiency of CH₃OCH₃ production, we turn off the reactions one by one. It appears that the gas-phase reactions (CH₃ + CH₃O and CH₃⁺ + CH₃OH) are inefficient and contribute almost negligibly to CH₃OCH₃ production. The s-CH₃ + s-CH₃O route is not efficient at low temperatures, since at 10 K neither s-CH₃ nor s-CH₃O are predicted to diffuse on ice using an $E_{\text{diffusion}} = (0.3-0.4) \times E_{\text{binding}}$.⁶⁸ Most of the CH₃OCH₃ present in the gas-phase arises from cosmic ray-induced desorption of s-CH₃OCH₃ produced by the C + s-CH₃OH (+ 2 s-H) reaction.

The main losses of gas-phase CH₃OCH₃ are through its reactions with He⁺, H₃⁺ and HCO⁺, through reactions with atomic C (this work) and the OH radical, and by depletion onto grains. The current model (dashed red line) underestimates the observed (hatched red rectangle) gas-phase abundance of CH₃OCH₃ shown in Figure 6. It should be noted that Nautilus uses the Minissale et al.⁶⁹ formalism for chemical desorption, which is based on experiments. As such, in the present simulations, only a very low percentage of CH₃OCH₃ molecules produced by the s-H + s-CH₃OCH₂ → CH₃OCH₃ reaction actually leads to desorption (10⁻⁴ %). The chemical desorption level would need to be approximately 3 % for the simulated CH₃OCH₃ abundance to reproduce the observed one. However, there are other non-thermal processes that could also be more efficient as well. As an example, for cosmic-ray induced sputtering, we use the experimental yields for pure water ices while measured yields for pure CO₂ ices are higher (see discussion in Wakelam et al. 2021).⁶⁴ This suggests that the yield for mixed ices is probably higher than the one we use.

The solid red line in Figure 6 shows the nominal abundance of CH₃OCH₃ generated by the model in the absence of the C + CH₃OCH₃ reaction.

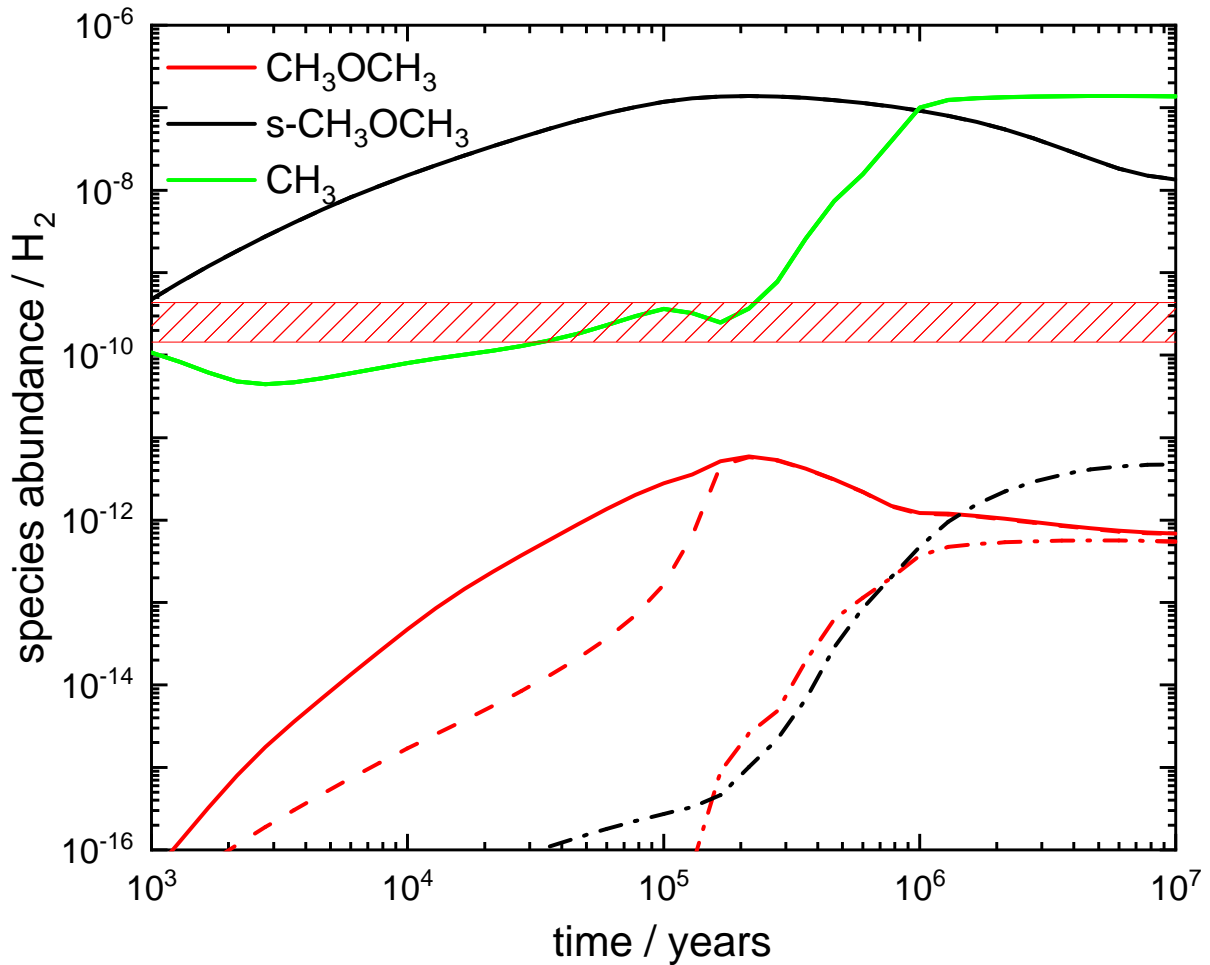


Figure 6 Gas-grain astrochemical model results for the formation of gas-phase CH_3OCH_3 (red lines), solid phase CH_3OCH_3 (black lines) and gas-phase CH_3 (green lines) in dark clouds as a function of cloud age. (Solid lines) standard network results. (dashed lines) the same network with the gas-phase $\text{C} + \text{CH}_3\text{OCH}_3$ reaction included. (Dashed-dotted line) new network without the $\text{C} + \text{s-CH}_3\text{OH}$ reaction. The horizontal red hatched rectangle represents the observed CH_3OCH_3 abundance in TMC-1²⁸ with an arbitrary error associated ($\pm\sqrt{3}$).

The inclusion of the $\text{C} + \text{CH}_3\text{OCH}_3$ reaction in the network with an estimated rate constant, $k_{\text{C}+\text{CH}_3\text{OCH}_3}(10\text{K}) = 1.3 \times 10^{-10} \text{ cm}^3 \text{ s}^{-1}$ leads to a maximum decrease of the CH_3OCH_3 abundance of more than an order of magnitude between 10^3 and 10^5 years as shown by the dashed red line in Figure 6. Increasing the estimated rate constant to $4.0 \times 10^{-10} \text{ cm}^3 \text{ s}^{-1}$, the value obtained by extrapolating the experimental fit to 10 K, leads to an additional threefold decrease of the CH_3OCH_3 abundance at short times. Given the experimental and theoretical results presented above, the formation of $\text{CH}_3 + \text{CH}_3 + \text{CO}$ was assumed to be the only product channel of this reaction during these simulations. Despite this, and the fact that two CH_3

radicals are produced for each CH_3OCH_3 consumed, the additional CH_3 produced by this reaction is small compared to other sources of CH_3 in dense interstellar clouds as the inclusion of this reaction induces a negligible change in the simulated CH_3 abundance (the solid and dashed green lines are indistinguishable in Figure 6). This reaction is also a negligible source of CO compared to other pathways already present in the model. At ages considered to be characteristic of typical dense clouds such as TMC-1 (a few 10^5 years), atomic carbon is removed from the gas-phase through reactions forming CO and by accretion onto grains, thereby limiting the effect of the $\text{C} + \text{CH}_3\text{OCH}_3$ reaction at longer times ($>10^5$ years). Despite the large effect of the $\text{C} + \text{CH}_3\text{OCH}_3$ reaction on CH_3OCH_3 abundances at early times, these simulations indicate that the $\text{C} + \text{CH}_3\text{OCH}_3$ reaction induces only small changes in the gas-phase CH_3OCH_3 abundance at typical dense interstellar cloud ages, with a calculated CH_3OCH_3 abundance that underestimates the observed one for TMC-1. When the $\text{C} + s\text{-CH}_3\text{OH}$ reaction is switched off, both the gas-phase (red dashed-dotted line) and solid phase (black dashed-dotted line) CH_3OCH_3 abundances fall by several orders of magnitude, showing the crucial role of this reaction. This also demonstrates the importance of Eley-Rideal reactions for CH_3OCH_3 , which, along with CH_3OH , $\text{C}_2\text{H}_5\text{OH}$, and H_2S , is a compound produced almost exclusively on grains. Its detection therefore enables us to better characterize the chemistry on grains in dense, cold regions, where COMs cannot a priori be synthesized in the same way as in protostars, since only atomic and molecular hydrogen are expected to be mobile on ice at 10 K. Furthermore, chemical desorption is assumed to be relatively inefficient for CH_3OCH_3 due to its size⁶⁹ and high binding energy ($4080 \pm 500 \text{ K}^{70}$), so its abundance in the gas phase is also a means of assessing the efficiency of desorption induced by cosmic-ray collisions.⁶⁴

6 Conclusions

This work describes the results of an experimental investigation of the $\text{C}(^3\text{P}) + \text{CH}_3\text{OCH}_3$ reaction, supported by theoretical calculations of the rate constant and product channels, followed by an astrochemical modeling study of its effects on interstellar chemistry. Experimentally, a supersonic flow reactor was used to investigate this process over the 50-296 K range. Pulsed laser photolysis was used for the in-situ generation of $\text{C}(^3\text{P})$ atoms, which were followed by pulsed laser induced fluorescence in the vacuum ultraviolet wavelength range. Theoretically, electronic structure calculations were performed on the ground $^3\text{A}'$ surface of $\text{C}_3\text{H}_6\text{O}$ to determine the various intermediates, transition states and product

channels involved. Based on the derived energies and structures, a master equation analysis was used to calculate rate constants and product branching ratios for this reaction as a function of temperature. The reaction is seen to accelerate as the temperature falls, while the low measured H-atom yields at all temperatures support the theoretical prediction that the major products should be $\text{CH}_3 + \text{CH}_3 + \text{CO}$. The $\text{C}(^3\text{P}) + \text{CH}_3\text{OCH}_3$ reaction was introduced into a gas-grain model of dense interstellar clouds. The simulations predict that CH_3OCH_3 abundances decrease significantly at intermediate times when gas-phase $\text{C}(^3\text{P})$ abundances are high, while the predicted CH_3OCH_3 abundances only reach high levels at later cloud ages when most of the $\text{C}(^3\text{P})$ has been locked up in interstellar reservoirs such as CO. Despite its high reactivity, the $\text{C}(^3\text{P}) + \text{CH}_3\text{OCH}_3$ reaction is likely to be only a very minor source of CH_3 in dense interstellar clouds.

Author information

Corresponding Author

Kevin M. Hickson – Institut des Sciences Moléculaires ISM, CNRS UMR 5255, Univ. Bordeaux, F-33400 Talence, France; orcid.org/0000-0001-8317-2606;

Email: kevin.hickson@u-bordeaux.fr

Authors

Jean-Christophe Loison – Institut des Sciences Moléculaires ISM, CNRS UMR 5255, Univ. Bordeaux, F-33400 Talence, France

Valentine Wakelam – Laboratoire d’astrophysique de Bordeaux, CNRS, Univ. Bordeaux, F 33615 Pessac, France

Supporting Information

Geometries and frequencies of the stationary points involved in the $\text{C}(^3\text{P}) + \text{CH}_3\text{OCH}_3$ reaction obtained at the M06-2X/aug-cc-pVTZ level of theory (DOCX). Energies, frequencies and rotational constants along the entrance channel leading to vdW1 formation. Reactions involved in CH_3OCH_3 production and destruction in the astrochemical network.

Acknowledgements

K.M.H. acknowledges support from the French program ‘Physique et Chimie du Milieu Interstellaire’ (PCMI) of the CNRS/INSU with the INC/INP cofunded by the CEA and CNES as well as funding from the ‘Program National de Planétologie’ (PNP) of the CNRS/INSU.

References

- (1) Schilke, P.; Keene, J.; Lebourlot, J.; Desforets, G. P.; Roueff, E. Atomic Carbon in a Dark Cloud - TMC-1. *Astron. Astrophys.* **1995**, *294*, L17-L20.
- (2) Ikeda, M.; Maezawa, H.; Ito, T.; Saito, G.; Sekimoto, Y.; Yamamoto, S.; Tatematsu, K.; Arikawa, Y.; Aso, Y.; Noguchi, T.; et al. Large-Scale Mapping Observations of the C I (3P_1 - 3P_0) and CO ($J = 3-2$) Lines Toward the Orion A Molecular Cloud. *Astrophys. J.* **1999**, *527*, L59-L62.
- (3) Ikeda, M.; Oka, T.; Tatematsu, K.; Sekimoto, Y.; Yamamoto, S. The Distribution of Atomic Carbon in the Orion Giant Molecular Cloud 1. *Astrophys. J., Suppl. Ser.* **2002**, *139*, 467.
- (4) Bensch, F. Neutral Carbon and CO Emission in the Core and the Halo of Dark Cloud Barnard 5. *Astron. Astrophys.* **2006**, *448*, 1043-1060.
- (5) Hickson, K. M.; Loison, J.-C.; Larregaray, P.; Bonnet, L.; Wakelam, V. An Experimental and Theoretical Investigation of the Gas-Phase $C(^3P) + N_2O$ Reaction. Low Temperature Rate Constants and Astrochemical Implications. *J. Phys. Chem. A* **2022**, *126*, 940-950.
- (6) McGuire, B. A. 2021 Census of Interstellar, Circumstellar, Extragalactic, Protoplanetary Disk, and Exoplanetary Molecules. *Astrophys. J., Suppl. Ser.* **2022**, *259*, 30.
- (7) Clary, D. C.; Haider, N.; Husain, D.; Kabir, M. Interstellar Carbon Chemistry: Reaction Rates of Neutral Atomic Carbon with Organic Molecules. *Astrophys. J.* **1994**, *422*, 416.
- (8) Clary, D. C.; Buonomo, E.; Sims, I. R.; Smith, I. W. M.; Geppert, W. D.; Naulin, C.; Costes, M.; Cartechini, L.; Casavecchia, P. $C + C_2H_2$: A Key Reaction in Interstellar Chemistry. *J. Phys. Chem. A* **2002**, *106*, 5541-5552.
- (9) Chastaing, D.; James, P. L.; Sims, I. R.; Smith, I. W. M. Neutral-Neutral Reactions at the Temperatures of Interstellar Clouds: Rate Coefficients for Reactions of Atomic Carbon, $C(^3P)$, with O_2 , C_2H_2 , C_2H_4 and C_3H_6 down to 15 K. *Phys. Chem. Chem. Phys.* **1999**, *1*, 2247-2256.
- (10) Chastaing, D.; Le Picard, S. D.; Sims, I. R.; Smith, I. W. M.; Geppert, W. D.; Naulin, C.; Costes, M. Rate Coefficients and Cross-Sections for the Reactions of $C(^3P_J)$ Atoms with Methylacetylene and Allene. *Chem. Phys. Lett.* **2000**, *331*, 170-176.
- (11) Kaiser, R. I.; Mebel, A. M. The Reactivity of Ground-State Carbon Atoms with Unsaturated Hydrocarbons in Combustion Flames and in the Interstellar Medium. *Int. Rev. Phys. Chem.* **2002**, *21*, 307-356.
- (12) Leonori, F.; Petrucci, R.; Segoloni, E.; Bergeat, A.; Hickson, K. M.; Balucani, N.; Casavecchia, P. Unraveling the Dynamics of the $C(^3P, ^1D) + C_2H_2$ Reactions by the Crossed Molecular Beam Scattering Technique. *J. Phys. Chem. A* **2008**, *112*, 1363-1379.
- (13) Costes, M.; Halvick, P.; Hickson, K. M.; Daugey, N.; Naulin, C. Non-Threshold, Threshold, and Nonadiabatic Behavior of the Key Interstellar $C + C_2H_2$ Reaction. *Astrophys. J.* **2009**, *703*, 1179-1187.
- (14) Naulin, C.; Daugey, N.; Hickson, K. M.; Costes, M. Dynamics of the Reactions of $C(^3P_J)$ Atoms with Ethylene, Allene, and Methylacetylene at Low Energy Revealed by Doppler-Fizeau Spectroscopy. *J. Phys. Chem. A* **2009**, *113*, 14447-14457.
- (15) Husain, D.; Ioannou, A. X. Reactions of Atomic Carbon, $C[2(^3P_J)]$, with Dienes and Diynes Investigated by Time-Resolved Atomic Resonance Absorption Spectroscopy in the Vacuum Ultraviolet. *J. Chem. Soc., Faraday Trans.* **1997**, *93*, 3625-3629.

- (16) Loison, J.-C.; Bergeat, A. Reaction of Carbon Atoms, C(2p², ³P) with C₃H₄ (Allene and Methylacetylene), C₃H₆ (Propylene) and C₄H₈ (Trans-Butene): Overall Rate Constants and Atomic Hydrogen Branching Ratios. *Phys. Chem. Chem. Phys.* **2004**, *6*, 5396-5401.
- (17) Husain, D.; Ioannou, A. X. Collisional Removal of Atomic Carbon, C[2p²(³P_J)], by Aldehydes and Ketones, Investigated by Time-Resolved Atomic Resonance Absorption Spectroscopy in the Vacuum Ultra-violet. *J. Photo. Photobio. A* **1999**, *129*, 1-7.
- (18) Haider, N.; Husain, D. The Collisional Behaviour of Ground State Atomic Carbon, C(2p² (³P_J)), with Unsaturated Cyclic Compounds Studied by Time-Resolved Atomic Resonance Absorption Spectroscopy in the Vacuum Ultra-Violet. *Bunsen-Ges. Phys. Chem., Ber.* **1993**, *97*, 571-576.
- (19) Herbst, E.; van Dishoeck, E. F. Complex Organic Interstellar Molecules. *Annu. Rev. Astron. Astrophys.* **2009**, 427-480.
- (20) Arce, H. G.; Santiago-García, J.; Jørgensen, J. K.; Tafalla, M.; Bachiller, R. Complex Molecules in the L1157 Molecular Outflow. *Astrophys. J.* **2008**, *681*, L21.
- (21) Öberg, K. I.; van der Marel, N.; Kristensen, L. E.; van Dishoeck, E. F. Complex Molecules Toward Low-Mass Protostars: The Serpens Core*. *Astrophys. J.* **2011**, *740*, 14.
- (22) Martín-Doménech, R.; Bergner, J. B.; Öberg, K. I.; Carpenter, J.; Law, C. J.; Huang, J.; Jørgensen, J. K.; Schwarz, K.; Wilner, D. J. Hot Corino Chemistry in the Class I Binary Source Ser-emb 11. *Astrophys. J.* **2021**, *923*, 155.
- (23) Bacmann, A.; Taquet, V.; Faure, A.; Kahane, C.; Ceccarelli, C. Detection of Complex Organic Molecules in a Prestellar Core: A New Challenge for Astrochemical Models. *Astron. Astrophys.* **2012**, *541*, L12.
- (24) Snyder, L. E.; Buhl, D.; Schwartz, P. R.; Clark, F. O.; Johnson, D. R.; Lovas, F. J.; Giguere, P. T. Radio Detection of Interstellar Dimethyl Ether. *Astrophys. J.* **1974**, *191*, L79.
- (25) Taquet, V.; López-Sepulcre, A.; Ceccarelli, C.; Neri, R.; Kahane, C.; Charnley, S. B. Constraining the Abundances of Complex Organics in the Inner Regions of Solar-Type Protostars. *Astrophys. J.* **2015**, *804*, 81.
- (26) Fuente, A.; Cernicharo, J.; Caselli, P.; McCoey, C.; Johnstone, D.; Fich, M.; van Kempen, T.; Palau, A.; Yıldız, U. A.; Tercero, B.; et al. The Hot Core towards the Intermediate-Mass Protostar NGC 7129 FIRS 2. *Astron. Astrophys.* **2014**, *568*, A65.
- (27) Rivilla, V. M.; Beltrán, M. T.; Cesaroni, R.; Fontani, F.; Codella, C.; Zhang, Q. Formation of Ethylene Glycol and other Complex Organic Molecules in Star-Forming Regions. *Astron. Astrophys.* **2017**, *598*, A59.
- (28) Agúndez, M.; Marcelino, N.; Tercero, B.; Cabezas, C.; de Vicente, P.; Cernicharo, J. O-Bearing Complex Organic Molecules at the Cyanopolyne Peak of TMC-1: Detection of C₂H₃CHO, C₂H₃OH, HCOOCH₃, and CH₃OCH₃. *Astron. Astrophys.* **2021**, *649*, L4.
- (29) Wakelam, V.; Loison, J. C.; Herbst, E.; Pavone, B.; Bergeat, A.; Béroff, K.; Chabot, M.; Faure, A.; Galli, D.; Geppert, W. D.; et al. The 2014 KIDA Network for Interstellar Chemistry. *Astrophys. J., Suppl. Ser.* **2015**, *217*, 20.
- (30) Balucani, N.; Ceccarelli, C.; Taquet, V. Formation of Complex Organic Molecules in Cold Objects: The Role of Gas-Phase Reactions. *Mon. Not. R. Astron. Soc.* **2015**, *449*, L16-L20.
- (31) Skouteris, D.; Balucani, N.; Ceccarelli, C.; Faginas Lago, N.; Codella, C.; Falcinelli, S.; Rosi, M. Interstellar Dimethyl Ether Gas-Phase Formation: A Quantum Chemistry and Kinetics Study. *Mon. Not. R. Astron. Soc.* **2019**, *482*, 3567-3575.
- (32) Ruaud, M.; Loison, J. C.; Hickson, K. M.; Gratier, P.; Hersant, F.; Wakelam, V. Modelling Complex Organic Molecules in Dense Regions: Eley-Rideal and Complex Induced Reaction. *Mon. Not. R. Astron. Soc.* **2015**, *447*, 4004-4017.

- (33) Daugey, N.; Caubet, P.; Retail, B.; Costes, M.; Bergeat, A.; Dorthe, G. Kinetic Measurements on Methylidyne Radical Reactions with Several Hydrocarbons at Low Temperatures. *Phys. Chem. Chem. Phys.* **2005**, *7*, 2921-2927.
- (34) Daugey, N.; Caubet, P.; Bergeat, A.; Costes, M.; Hickson, K. M. Reaction Kinetics to Low Temperatures. Dicarbon + Acetylene, Methylacetylene, Allene and Propene from $77 \leq T \leq 296$ K. *Phys. Chem. Chem. Phys.* **2008**, *10*, 729-737.
- (35) Hickson, K. M.; Loison, J.-C.; Lique, F.; Kłos, J. An Experimental and Theoretical Investigation of the $C(^1D) + N_2 \rightarrow C(^3P) + N_2$ Quenching Reaction at Low Temperature. *J. Phys. Chem. A* **2016**, *120*, 2504-2513.
- (36) Hickson, K., M.; Loison, J.-C.; Bourgalais, J.; Capron, M.; Le Picard, S., D.; Goulay, F.; Wakelam, V. The $C(^3P) + NH_3$ Reaction in Interstellar Chemistry. II. Low Temperature Rate Constants and Modeling of NH, NH_2 , and NH_3 Abundances in Dense Interstellar Clouds. *Astrophys. J.* **2015**, *812*, 107.
- (37) Hickson, K. M.; San Vicente Veliz, J. C.; Koner, D.; Meuwly, M. Low-Temperature Kinetics for the N + NO Reaction: Experiment Guides the Way. *Phys. Chem. Chem. Phys.* **2023**, *25*, 13854-13863.
- (38) Grondin, R.; Loison, J.-C.; Hickson, K. M. Low Temperature Rate Constants for the Reactions of $O(^1D)$ with N_2 , O_2 , and Ar. *J. Phys. Chem. A* **2016**, *120*, 4838-4844.
- (39) Nuñez-Reyes, D.; Loison, J.-C.; Hickson, K. M.; Dobrijevic, M. A Low Temperature Investigation of the $N(^2D) + CH_4$, C_2H_6 and C_3H_8 reactions. *Phys. Chem. Chem. Phys.* **2019**, *21*, 6574-6581.
- (40) Rowe, B.R.; Canosa, A.; Heard D.E. *Uniform Supersonic Flows in Chemical Physics: Chemistry close to Absolute Zero Studied using the CRESU Method*; World Scientific, 2022.
- (41) Zhao, Y.; Truhlar, D. The M06 Suite of Density Functionals for Main Group Thermochemistry, Thermochemical Kinetics, Noncovalent Interactions, Excited States, and Transition Elements: Two New Functionals and Systematic Testing of Four M06-Class Functionals and 12 Other Functionals. *Theor. Chem. Acc.* **2008**, *120*, 215-241.
- (42) Guo, Y.; Riplinger, C.; Becker, U.; Liakos, D. G.; Minenkov, Y.; Cavallo, L.; Neese, F. Communication: An Improved Linear Scaling Perturbative Triples Correction for the Domain Based Local Pair-Natural Orbital Based Singles and Doubles Coupled Cluster Method [DLPNO-CCSD(T)]. *J. Chem. Phys.* **2018**, *148*, 011101.
- (43) Neese, F. The ORCA Program System. *WIREs Comput. Mol. Sci.* **2012**, *2*, 73-78.
- (44) Neese, F. Software update: The ORCA program system—Version 5.0. *WIREs Comput. Mol. Sci.* **2022**, *12*, e1606.
- (45) Hanwell, M. D.; Curtis, D. E.; Lonie, D. C.; Vandermeersch, T.; Zurek, E.; Hutchison, G. R. Avogadro: An Advanced Semantic Chemical Editor, Visualization, and Analysis Platform. *J. Cheminf.* **2012**, *4*, 17.
- (46) Recio, P.; Alessandrini, S.; Vanuzzo, G.; Pannacci, G.; Baggioli, A.; Marchione, D.; Caracciolo, A.; Murray, V. J.; Casavecchia, P.; Balucani, N.; et al. Intersystem Crossing in the Entrance Channel of the Reaction of $O(^3P)$ with Pyridine. *Nat. Chem.* **2022**, *14*, 1405-1412.
- (47) Barker, J. R. Multiple-Well, Multiple-Path Unimolecular Reaction Systems. I. MultiWell Computer Program Suite. *Int. J. Chem. Kinet.* **2001**, *33*, 232-245.
- (48) Barker, J. R.; Nguyen, T. L.; Stanton, J. F.; Aieta, C.; Ceotto, M.; Gabas, F.; Kumar, T. J. D.; Li, C. G. L.; Lohr, L. L.; Maranzana, A. et al., MultiWell-2022 Software Suite, J. R. Barker, University of Michigan, Ann Arbor, Michigan, USA, **2022**; <https://multiwell.engin.umich.edu>.
- (49) Miller, W. H., Unified Statistical Model for "Complex" and "Direct" Reaction Mechanisms. *J. Chem. Phys.* **1976**, *65*, 2216-2223.

- (50) Ali, M. A.; Sonk, J. A.; Barker, J. R., Predicted Chemical Activation Rate Constants for HO₂ + CH₂NH: The Dominant Role of a Hydrogen-Bonded Pre-Reactive Complex. *J. Phys. Chem. A* **2016**, *120*, 7060-7070.
- (51) Weaver, A. B.; Alexeenko, A. A., Revised Variable Soft Sphere and Lennard-Jones Model Parameters for Eight Common Gases up to 2200 K. *J. Phys. Chem. Ref. Data* **2015**, *44*, 023103.
- (52) Barker, J. R.; Yoder, L. M.; King, K. D., Vibrational Energy Transfer Modeling of Nonequilibrium Polyatomic Reaction Systems. *J. Phys. Chem. A* **2001**, *105*, 796-809.
- (53) Shannon, R. J.; Cossou, C.; Loison, J.-C.; Caubet, P.; Balucani, N.; Seakins, P. W.; Wakelam, V.; Hickson, K. M. The Fast C(³P) + CH₃OH Reaction as an Efficient Loss Process for Gas-Phase Interstellar Methanol. *RSC Adv.* **2014**, *4*, 26342-26353.
- (54) Hickson, K. M.; Loison, J.-C.; Wakelam, V. Kinetic Study of the Gas-Phase C(³P) + CH₃CN Reaction at Low Temperatures: Rate Constants, H-Atom Product Yields, and Astrochemical Implications. *ACS Earth Space Chem.* **2021**, *5*, 824-833.
- (55) Hickson, K. M.; Loison, J.-C.; Wakelam, V. Kinetic Study of the Gas-Phase Reaction between Atomic Carbon and Acetone: Low-Temperature Rate Constants and Hydrogen Atom Product Yields. *ACS Earth Space Chem.* **2023**, *7*, 2091-2104.
- (56) Bergeat, A.; Loison, J.-C. Reaction of Carbon Atoms, C(2p2, ³P) with C₂H₂, C₂H₄ and C₆H₆: Overall Rate Constant and Relative Atomic Hydrogen Production. *Phys. Chem. Chem. Phys.* **2001**, *3*, 2038-2042.
- (57) Le, T. N.; Lee, H.-y.; Mebel, A. M.; Kaiser, R. I. Ab Initio MO Study of the Triplet C₃H₄ Potential Energy Surface and the Reaction of C(³P) with Ethylene, C₂H₄. *J. Phys. Chem. A* **2001**, *105*, 1847-1856.
- (58) Hickson, K. M.; Loison, J.-C.; Nuñez-Reyes, D.; Méreau, R. Quantum Tunneling Enhancement of the C + H₂O and C + D₂O Reactions at Low Temperature. *J. Phys. Chem. Lett.* **2016**, *7*, 3641-3646.
- (59) Nuñez-Reyes, D.; Hickson, K. M. Kinetic and Product Study of the Reactions of C(¹D) with CH₄ and C₂H₆ at Low Temperature. *J. Phys. Chem. A* **2017**, *121*, 3851-3857.
- (60) Tennis, J.; Loison, J.-C.; Herbst, E. Radiative Association between Neutral Radicals in the Interstellar Medium: CH₃ + CH₃O. *Astrophys. J.* **2021**, *922*, 133.
- (61) Ruaud, M.; Wakelam, V.; Hersant, F. Gas and Grain Chemical Composition in Cold Cores as Predicted by the Nautilus Three-Phase Model. *Mon. Not. R. Astron. Soc.* **2016**, *459*, 3756-3767.
- (62) Manigand, S.; Coutens, A.; Loison, J. C.; Wakelam, V.; Calcutt, H.; Müller, H. S. P.; Jørgensen, J. K.; Taquet, V.; Wampfler, S. F.; Bourke, T. L.; et al. The ALMA-PILS Survey: First Detection of the Unsaturated 3-Carbon Molecules Propenal (C₂H₃CHO) and Propylene (C₃H₆) Towards IRAS 16293–2422 B. *Astron. Astrophys.* **2021**, *645*, A53.
- (63) Coutens, A.; Loison, J.-C.; Boulanger, A.; Caux, E.; Müller, H. S. P.; Wakelam, V.; Manigand, S.; Jørgensen, J. K. The ALMA-PILS survey: First Tentative Detection of 3-hydroxypropenal (HOCHCHCHO) in the Interstellar Medium and Chemical Modeling of the C₃H₄O₂ Isomers. *Astron. Astrophys.* **2022**, *660*, L6.
- (64) Wakelam, V.; Dartois, E.; Chabot, M.; Spezzano, S.; Navarro-Almida, D.; Loison, J.-C.; Fuente, A. Efficiency of Non-Thermal Desorptions in Cold-Core Conditions. *Astron. Astrophys.* **2021**, *652*, A63.
- (65) Jarrold, M. F.; Kirchner, N. J.; Liu, S.; Bowers, M. T. Metastable and Collision-Induced Dissociation Studies of Unimolecular and Bimolecular Reactions in the C₂H₅O⁺, C₂H₇O⁺, and C₂H₈N⁺ Systems: the Role of Methyl (CH₃⁺) Radiative Association Reactions in Interstellar Clouds. *J. Phys. Chem.* **1986**, *90*, 78-83.

- (66) Herbst, E. Can Gas Phase Reactions Produce Complex Oxygen-Containing Molecules. *Astrophys. J.* **1987**, *313*, 867-876.
- (67) Hamberg, M.; Zhaunerchyk, V.; Vignen, E.; Kaminska, M.; Kashperka, I.; Zhang, M.; Trippel, S.; Österdahl, F.; af Ugglas, M.; Thomas, R. D.; et al. Experimental Studies of the Dissociative Recombination of CD_3CDOD^+ and $\text{CH}_3\text{CH}_2\text{OH}_2^+$. *Astron. Astrophys.* **2010**, *522*, A90.
- (68) Hasegawa, T. I.; Herbst, E.; Leung, C. M. Models of gas-grain chemistry in dense interstellar clouds with complex organic molecules. *ApJS* **1992**, *82*, 167-195.
- (69) Minissale, M.; Dulieu, F.; Cazaux, S.; Hocuk, S. Dust as Interstellar Catalyst. *Astron. Astrophys.* **2016**, *585*, A24.
- (70) Lattalais, M.; Bertin, M.; Mokrane, H.; Romanzin, C.; Michaut, X.; Jeseck, P.; Fillion, J.-H.; Chaabouni, H.; Congiu, E.; Dulieu, F.; et al. Differential Adsorption of Complex Organic Molecules Isomers at Interstellar Ice Surfaces. *Astron. Astrophys.* **2011**, *532*, A12.

Supporting information file for

A Low Temperature Kinetic Study of the C(³P) + CH₃OCH₃ Reaction. Rate constants, H-atom Product

Yields and Astrochemical Implications

Kevin M. Hickson,^{1,*} Jean-Christophe Loison,¹ and Valentine Wakelam²

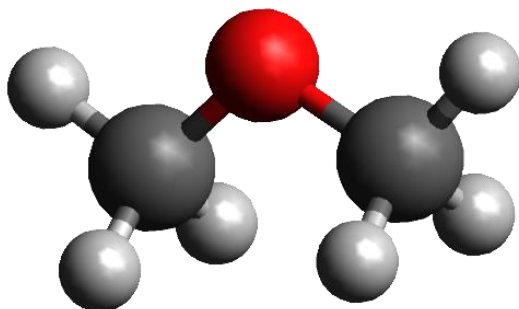
¹Institut des Sciences Moléculaires ISM, CNRS UMR 5255, Univ. Bordeaux, 351 Cours de la Libération, F-33400, Talence, France

²Laboratoire d'astrophysique de Bordeaux, CNRS, Univ. Bordeaux, B18N, allée Geoffroy Saint-Hilaire, F-33615 Pessac, France

Geometries and frequencies of the stationary points involved in the C(³P) + CH₃OCH₃ reaction obtained at the M06-2X/aug-cc-pVTZ level of theory.

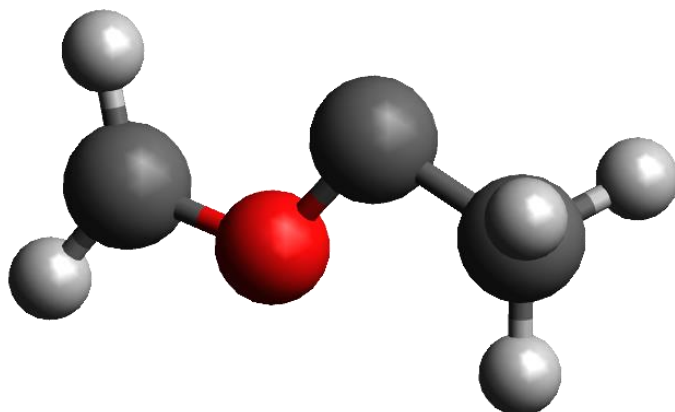
Geometries in Cartesian coordinates

Reactants and products



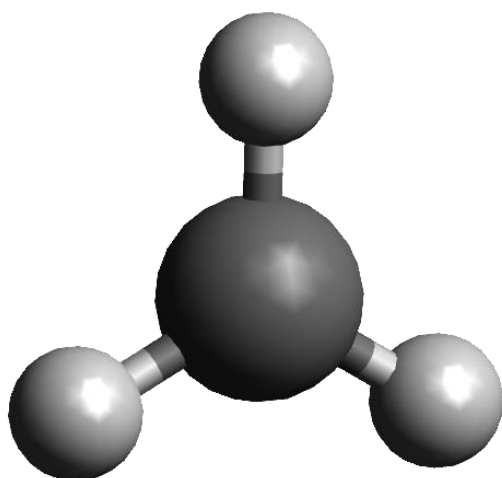
CH₃OCH₃

O	0.000001	0	0.593687
C	0	1.161471	-0.19451
C	0	-1.16147	-0.19451
H	0	2.018972	0.47384
H	-1E-06	-2.01897	0.47384
H	0.889393	1.203788	-0.83341
H	-0.8894	1.203787	-0.83341
H	-0.88939	-1.20379	-0.83341
H	0.889395	-1.20379	-0.83341



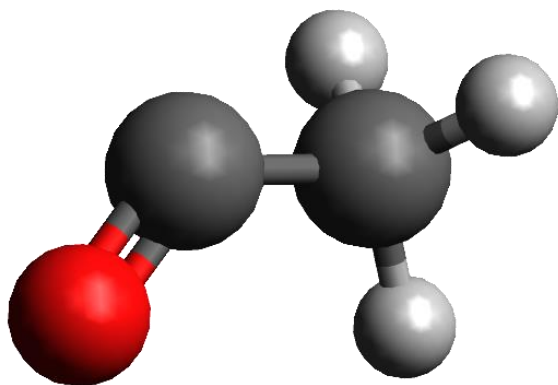
CH₂OCCH₃

O	0.551426	-0.39739	-0.27947
C	2.746494	0.172572	-0.24953
H	3.135243	1.051678	0.269798
H	2.534392	0.406786	-1.29474
H	3.541063	-0.5747	-0.17941
C	-0.62904	-0.84545	0.219614
H	-1.44037	-0.86737	-0.48349
H	-0.65566	-1.12591	1.258285
C	1.58632	-0.33807	0.533893



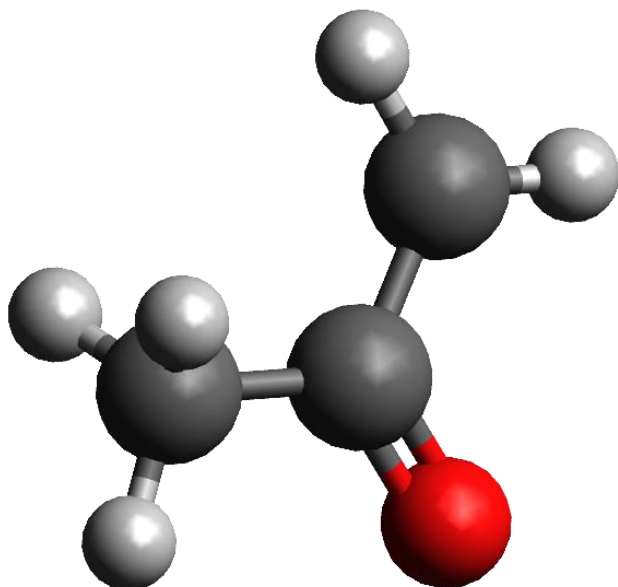
CH₃

C	-0.70372	1.186541	-5.8E-05
H	-0.70393	0.222151	-0.4783
H	-0.70309	2.083072	-0.5959
H	-0.70309	1.254814	1.074252



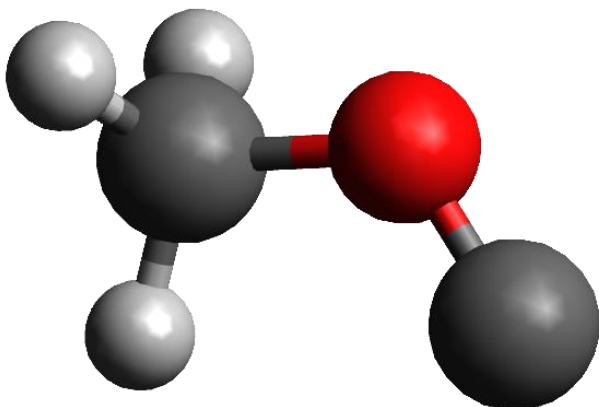
CH₃CO

O	-0.74553	1.29281	-0.37691
C	1.59815	0.710808	-0.23507
H	2.270581	1.396212	0.277147
H	1.66455	0.838353	-1.31566
H	1.875973	-0.30075	0.053802
C	0.194665	0.976079	0.248945



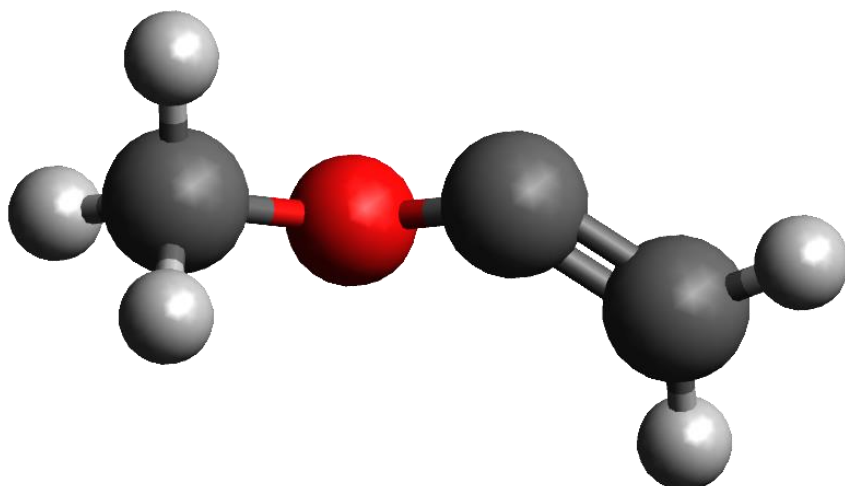
CH₃COCH₂

C	-0.00086	0.148935	-1E-06
O	0.427942	1.295073	0
C	-1.41953	-0.09936	0
C	0.925689	-1.04507	0
H	-2.09164	0.744823	0.000001
H	-1.81879	-1.10279	0.000001
H	1.956691	-0.70529	0.000001
H	0.742514	-1.66434	0.878793
H	0.742516	-1.66434	-0.87879



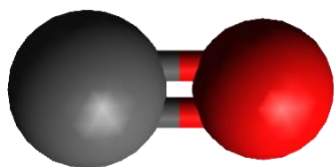
CH₃O

O	-1.19467	0.827273	0.165282
C	-1.2939	-0.63672	0.061527
H	-2.33199	-0.89373	0.245446
H	-0.97396	-0.9334	-0.93311
H	-0.65161	-1.0475	0.833542
C	-0.82459	1.5167	-0.81057



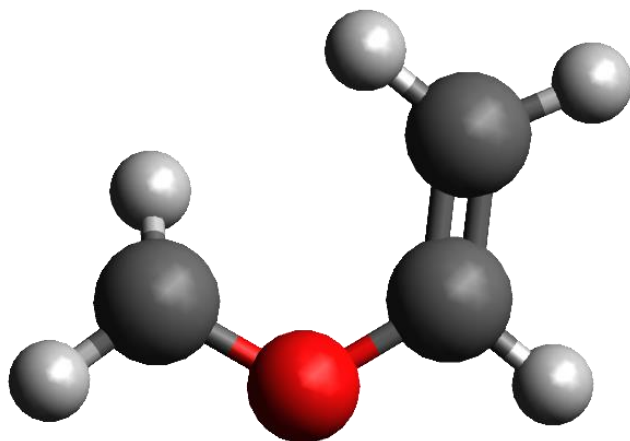
CH₃OCCH₂

O	0.161042	-0.23304	-0.30566
C	2.429567	0.532216	-0.17579
H	3.184404	0.937174	0.479557
H	2.650462	0.432194	-1.23393
C	-0.47068	-1.37802	0.268988
H	-1.3652	-1.56093	-0.31741
H	0.19694	-2.23791	0.217179
H	-0.73476	-1.17677	1.306307
C	1.263118	0.162634	0.300079



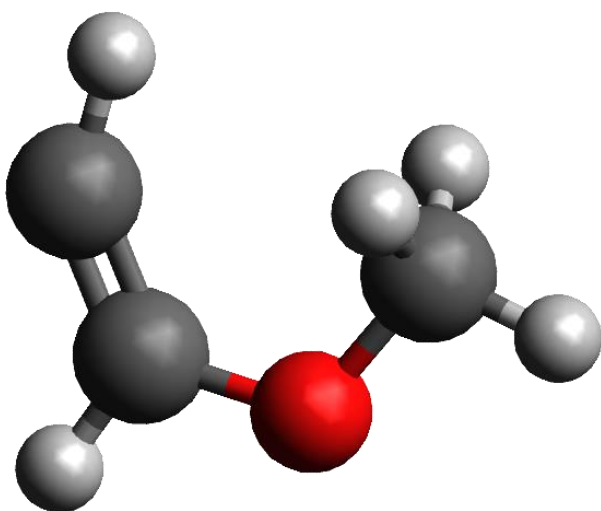
CO

C	0	0	-0.64096
O	0	0	0.48043



H₂CCHOCH₂

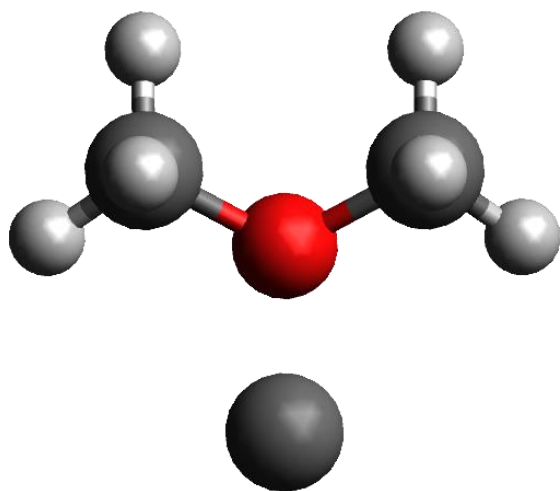
O	-0.05854	0.727316	-0.92497
C	1.063769	1.123118	-0.28273
H	1.518344	0.429444	0.410454
H	-0.22661	0.024127	1.710468
H	1.648896	1.827412	-0.84876
C	-0.92978	-0.0959	-0.28051
H	-1.66007	-0.48288	-0.97628
C	-0.93135	-0.39617	1.009659
H	-1.6862	-1.07023	1.381944



HCCHOCH₃

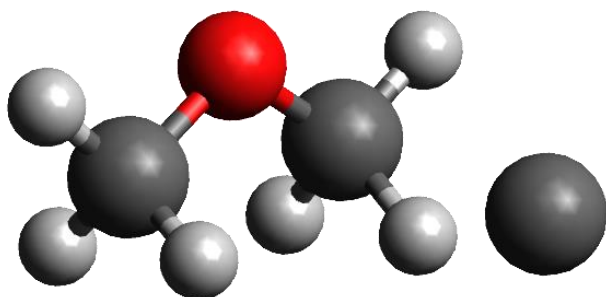
O	-0.24377	0.83835	-0.81111
C	0.792658	0.960075	0.140836
H	1.322449	0.011188	0.255287
H	0.390034	1.263507	1.110362
H	1.472095	1.720253	-0.2315
C	-1.19959	-0.07796	-0.50774
H	-1.95733	-0.1116	-1.28173
C	-1.26748	-0.85071	0.54927
H	-0.73935	-1.07846	1.455183

Intermediates



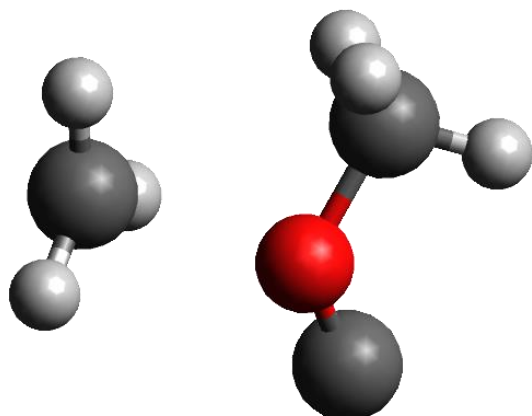
vdW1

O	-0.26659	0.54844	0.21022
C	1.14860	0.36722	0.10533
H	1.59007	1.35258	0.20868
H	1.38446	-0.05085	-0.87365
H	1.47375	-0.29362	0.90761
C	-1.00595	-0.67221	0.10351
H	-2.05170	-0.40467	0.20867
H	-0.82900	-1.11479	-0.87729
H	-0.69111	-1.34134	0.90309
C	-0.79345	1.63044	-0.91095



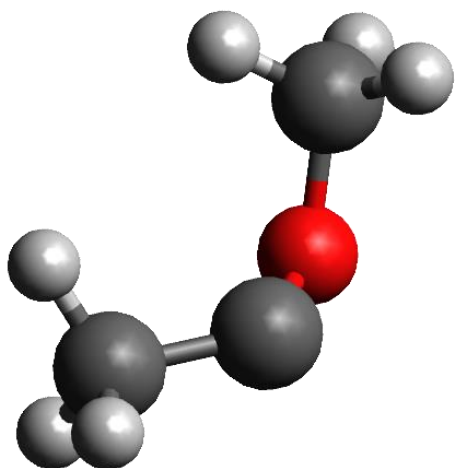
vdW2

O	-0.51334	-0.49696	-0.44761
C	0.57429	-0.73610	0.35195
H	1.27161	-1.39343	-0.15486
H	0.30726	-1.11509	1.34673
H	1.12119	0.24206	0.63062
C	-1.42541	0.41718	0.12415
H	-2.24191	0.53999	-0.58097
H	-1.81405	0.03554	1.07330
H	-0.93822	1.38224	0.29170
C	1.93374	1.16608	-0.22665



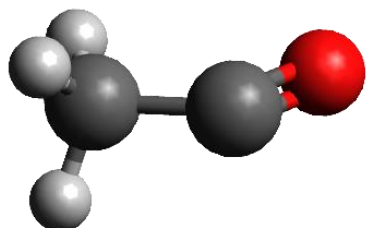
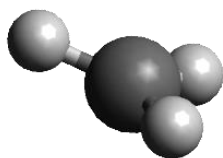
INT1

O	-0.24338	0.032625	-0.41511
C	3.016732	-0.40236	-0.16901
H	2.80868	0.226502	0.680798
H	2.84071	-0.0254	-1.16271
H	3.522668	-1.34371	-0.03366
C	-0.14455	-1.29644	0.207091
H	-1.14962	-1.70537	0.229
H	0.507696	-1.88828	-0.42708
H	0.26989	-1.17913	1.204689
C	0.0974	1.060938	0.209318



INT2

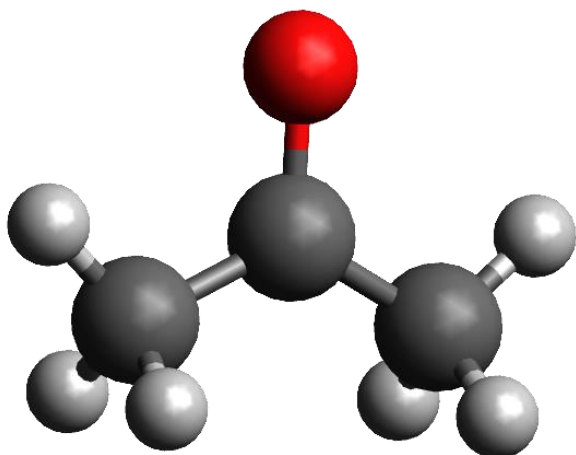
O	0.175388	-0.18571	-0.29806
C	2.659922	0.025238	-0.18774
H	3.37031	0.546367	0.449877
H	2.812139	0.362351	-1.21857
H	2.891744	-1.04549	-0.14677
C	-0.31777	-1.40382	0.265628
H	-1.19506	-1.6856	-0.3096
H	0.439882	-2.18577	0.194679
H	-0.58735	-1.24886	1.309958
C	1.277035	0.300663	0.263914



INT3

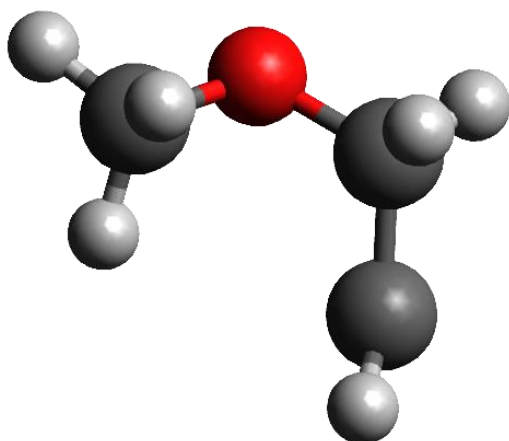
O	0.517289	1.374719	-0.0459
C	2.46384	-0.06113	-0.1464
H	3.404359	0.487115	-0.09612
H	2.20977	-0.29273	-1.18109
H	2.568706	-0.97075	0.439229
C	-0.23121	-1.9529	0.214698
H	-0.69881	-1.30552	-0.50756

H	0.183244	-2.89778	-0.09438
H	-0.29303	-1.71062	1.262621
C	1.402083	0.808978	0.478215



INT4

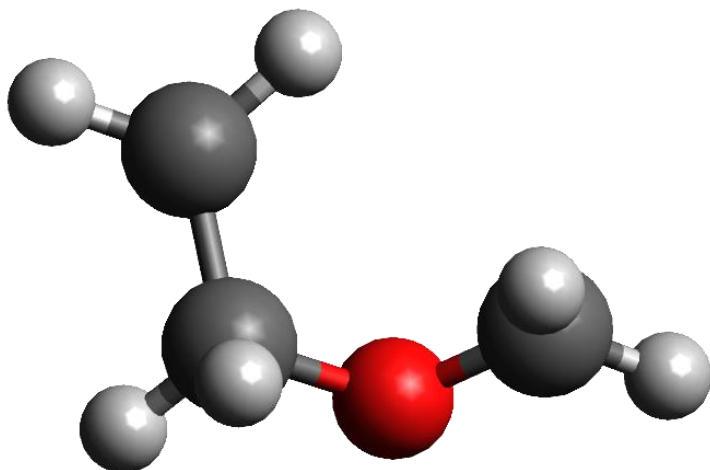
O	-0.52382	0.000035	1.286584
C	0.039028	1.297329	-0.6047
H	0.2591	2.14577	0.039953
H	-0.97073	1.425227	-1.0119
H	0.750732	1.28674	-1.42789
C	0.038923	-1.29734	-0.60467
H	0.25892	-2.14578	0.039992
H	-0.97085	-1.42516	-1.01188
H	0.750631	-1.28682	-1.42786
C	0.157373	-1E-06	0.152863



INT5

O	-0.05182	0.63939	-0.82779
C	0.944503	0.932093	0.121977
H	1.694207	0.133354	0.164145
H	0.520113	1.069367	1.120795
H	1.425671	1.855491	-0.18964

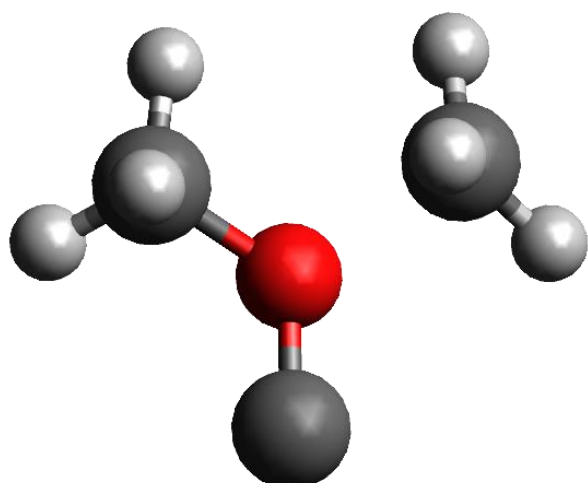
C	-0.6804	-0.60976	-0.60302
H	-1.37364	-0.73844	-1.43578
H	0.070237	-1.41443	-0.6673
C	-1.39337	-0.71894	0.678332
H	-1.1555	-1.14813	1.63829



INT6

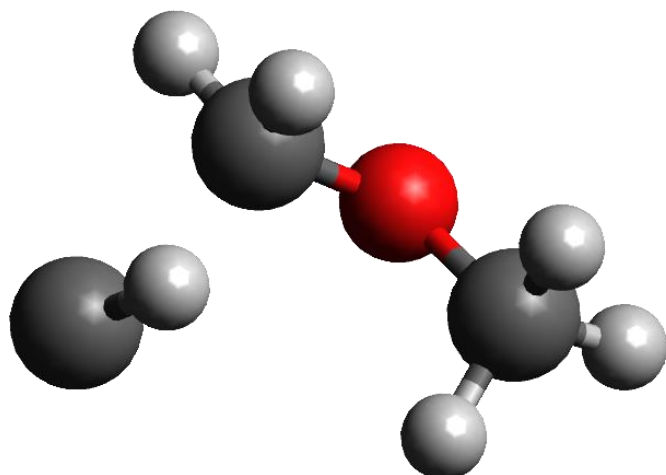
O	0.002364	0.738851	-0.87612
C	1.184886	1.083496	-0.32577
H	1.827686	0.290614	0.038045
H	-0.37447	0.101303	1.695535
H	1.592788	2.006234	-0.70372
C	-0.52202	-0.50687	-0.44014
H	-1.3734	-0.71721	-1.08671
H	0.234409	-1.28406	-0.63461
C	-0.92349	-0.49986	0.987307
H	-1.64875	-1.21251	1.346183

Transition states



TS1

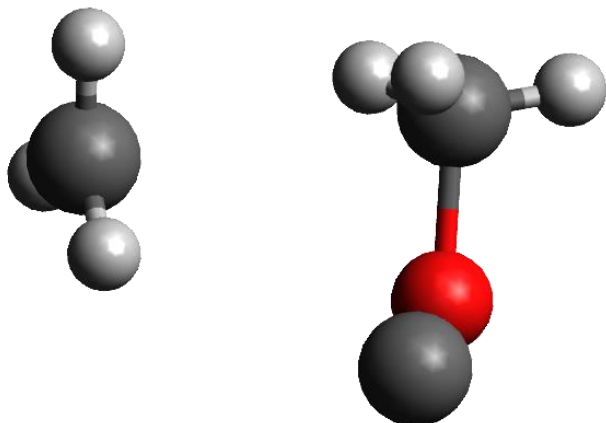
O	-0.43194	0.652197	0.138771
C	1.346134	0.341825	0.125032
H	1.66682	1.371761	0.16482
H	1.47063	-0.15042	-0.83015
H	1.549757	-0.25407	1.004669
C	-1.0735	-0.65659	0.061652
H	-2.13039	-0.49503	0.242225
H	-0.91372	-1.06891	-0.9319
H	-0.63119	-1.2776	0.835186
C	-0.85261	1.536841	-0.8103



TS2

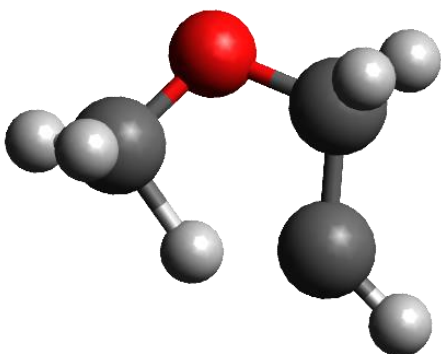
O	-0.47366	-0.42744	-0.49836
C	0.61526	-0.66692	0.260534
H	1.306684	-1.34978	-0.21948
H	0.388403	-0.94561	1.295384
H	1.181381	0.561942	0.814434
C	-1.43246	0.413358	0.119738

H	-2.27849	0.482323	-0.55593
H	-1.75466	-0.01019	1.074737
H	-1.00396	1.405783	0.278836
C	1.844556	0.774067	-0.14369



TS3

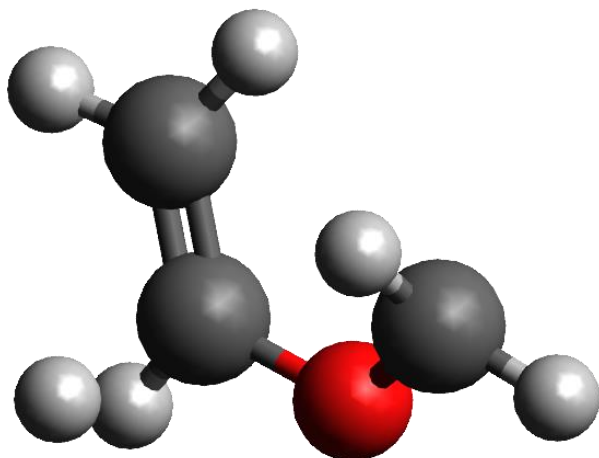
O	-0.39575	0.221184	-0.2275
C	3.084431	-0.37305	-0.16568
H	2.941806	0.581687	0.311339
H	3.075864	-0.44235	-1.24055
H	3.365671	-1.23004	0.423136
C	-0.16581	-1.4031	0.140421
H	-1.17542	-1.77848	0.239528
H	0.370431	-1.77904	-0.72075
H	0.411258	-1.3937	1.056993
C	0.013751	1.076255	0.506387



TS4

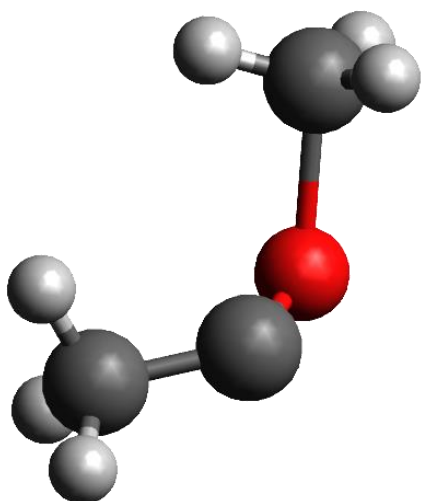
O	0.20203	0.472492	-1.02909
C	0.980231	0.92593	0.020068
H	1.899862	0.3616	0.187099
H	0.185643	0.506161	1.011347
H	1.110064	2.00249	-0.00419
C	-0.58395	-0.64044	-0.59673
H	-1.50502	-0.63632	-1.1833
H	-0.05056	-1.57843	-0.8119

C	-0.78636	-0.45829	0.859657
H	-1.45194	-0.9552	1.547035



TS5

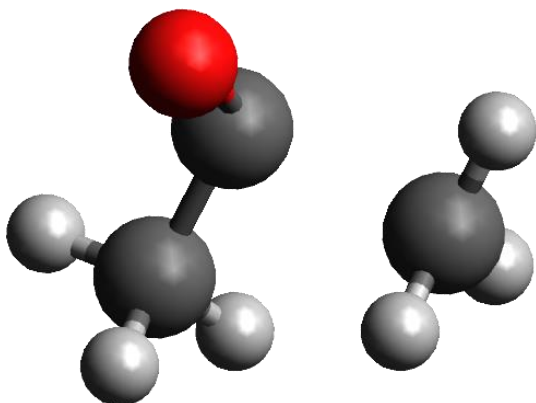
O	0.016701	0.717049	-0.94624
C	1.122	1.132194	-0.28903
H	1.624442	0.408603	0.339554
H	-0.23769	0.062384	1.674745
H	1.655462	1.913396	-0.80248
C	-0.74723	-0.24852	-0.36569
H	-1.44365	-0.66698	-1.07783
H	0.401142	-1.64261	-0.80326
C	-0.85139	-0.4622	0.958595
H	-1.53979	-1.21332	1.311648



TS6

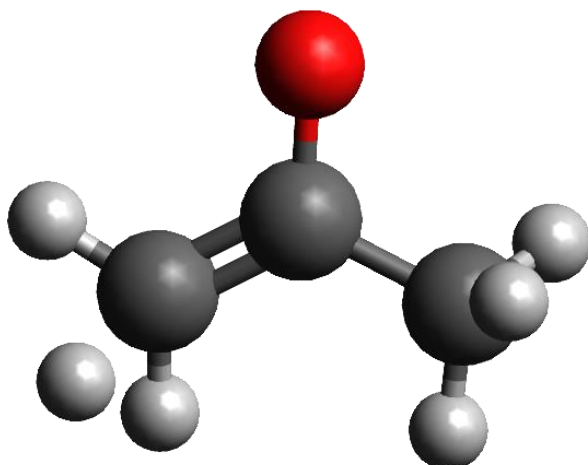
O	-0.87972	0.682262	-0.24887
C	1.56661	0.731278	-0.2159
H	2.294426	1.361268	0.28737
H	1.641276	0.873882	-1.29676
H	1.803512	-0.31354	0.011272

C	-1.58832	-0.95175	0.258798
H	-2.46344	-0.98718	-0.37146
H	-0.79403	-1.63912	0.005092
H	-1.7636	-0.79068	1.311788
C	0.183295	1.033568	0.258667



TS7

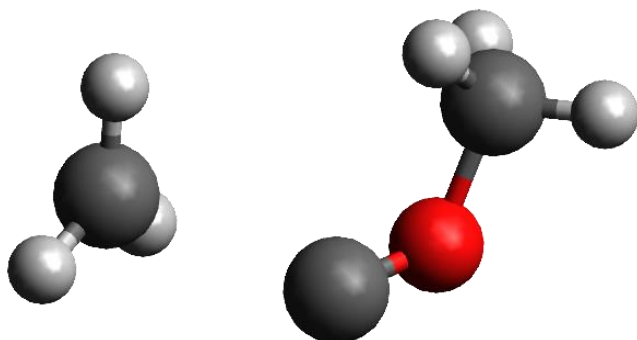
O	3.23492	2.679907	-0.76783
C	4.017871	0.476388	-0.14086
H	5.076618	0.700087	-0.01174
H	3.8565	0.085399	-1.14763
H	3.716865	-0.25183	0.604467
C	3.280057	1.798369	0.053862
C	1.353225	1.091544	0.013159
H	1.308233	0.590138	-0.94347
H	0.812076	2.020948	0.096365
H	1.388184	0.469147	0.895935



TS8

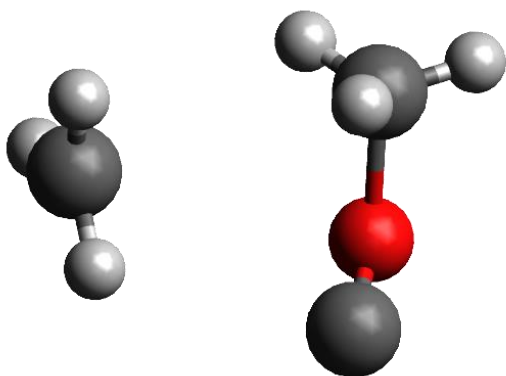
O	-0.57533	-0.07514	1.299034
C	0.334228	1.193075	-0.42935
H	0.285126	2.099957	0.154239
H	-1.2592	1.825553	-1.44391

H	0.916221	1.191042	-1.33705
C	0.025478	-1.31874	-0.59877
H	0.593326	-2.0277	0.001587
H	-0.97759	-1.71887	-0.7471
H	0.501173	-1.18242	-1.56624
C	-0.05413	0.013241	0.098047



TS9

O	-0.04908	-0.14549	-0.33582
C	3.139505	-0.03853	-0.15727
H	3.499054	0.885822	0.259448
H	2.973644	-0.11271	-1.21892
H	3.153126	-0.93182	0.445075
C	-0.39772	-1.47651	0.16184
H	-1.48119	-1.54084	0.177343
H	0.019391	-2.1946	-0.53793
H	0.024385	-1.59735	1.156219
C	0.645114	0.631409	0.37334



TS10

O	-0.83748	1.535309	-0.3447
C	1.850629	0.638001	-0.29398
H	2.272172	1.470237	0.249679
H	1.717009	0.75892	-1.35855
H	2.071384	-0.35124	0.074191
C	-0.21532	0.862284	0.325617

Table S1 Reactants and products (frequencies in cm⁻¹)

CH ₃ OCH ₃	CH ₂ OCCH ₃	CH ₃	CH ₃ CO	CH ₃ COCH ₂	CH ₃ OC	CH ₃ OCCH ₂	CO	H ₂ CCHOCH ₂	HCCHOCH ₃
236	51	432	107	22	101	112	2271	223	247
268	175	1412	469	369	475	160		321	275
430	238	1413	867	388	824	320		374	314
984	340	3144	957	518	1132	492		591	558
1135	376	3321	1050	533	1159	677		652	649
1177	576	3323	1354	741	1381	851		725	849
1207	901		1461	837	1483	911		886	928
1235	913		1463	933	1490	1078		930	983
1278	1114		1987	1030	1528	1172		1007	1187
1462	1140		3066	1070	3095	1181		1111	1187
1492	1194		3165	1285	3204	1258		1212	1240
1495	1309		3169	1397	3209	1408		1297	1340
1503	1366			1464		1480		1384	1474
1509	1451			1481		1502		1426	1499
1526	1454			1482		1510		1492	1513
3013	1479			1675		1746		1715	1674
3020	3039			3073		3070		3162	3044
3064	3115			3139		3144		3205	3105
3071	3133			3180		3145		3237	3179
3159	3201			3189		3189		3296	3193
3161	3365			3295		3266		3308	3319

Table S2 Intermediates (frequencies in cm⁻¹)

vdW1	vdW2	INT1	INT2	INT3	INT4	INT5	INT6
154	93	46	81	71	168	125	92
240	173	77	140	76	180	203	154
328	218	102	149	88	315	240	276
347	270	119	403	100	359	374	378
387	415	122	454	127	379	543	425
506	455	162	881	147	806	745	517
918	992	199	1021	189	959	942	602
1091	1048	479	1042	469	964	1059	836
1168	1148	510	1094	495	978	1088	958
1207	1196	825	1171	864	1101	1166	1065
1215	1235	1129	1200	956	1162	1185	1118
1279	1278	1164	1351	1052	1279	1222	1195
1455	1344	1380	1390	1352	1374	1307	1291
1475	1455	1410	1465	1410	1400	1374	1311
1489	1493	1416	1472	1415	1463	1464	1402
1494	1498	1484	1489	1452	1476	1481	1452
1497	1511	1488	1500	1463	1479	1498	1476
1513	1537	1524	1504	1983	1501	1515	1506
3069	2344	3093	3009	3064	3019	2963	2962
3074	3026	3137	3059	3140	3021	3019	3114
3156	3034	3200	3060	3155	3121	3078	3140
3157	3096	3206	3134	3177	3122	3095	3187
3203	3178	3313	3154	3315	3165	3161	3291
3206	3197	3316	3176	3320	3166	3264	3296

Table S3 Transition states (frequencies in cm⁻¹)

TS1	TS2	TS3	TS4	TS5	TS6	TS7	TS8	TS9	TS10
-1034	-713	-845	-1950	-873	-861	-543	-1804	-144	-415
179	121	44	-289	210	13	16	180	53	48
222	182	81	191	323	75	200	230	62	272
303	242	104	381	359	136	253	269	90	512
342	407	110	619	446	379	353	305	179	556
444	456	150	706	493	448	436	400	258	891
783	616	210	851	595	726	608	538	262	1421
833	860	279	963	665	765	637	715	487	1427
875	997	448	997	698	911	843	876	566	2120
982	1145	523	1095	845	980	968	885	861	3124
1152	1185	897	1107	929	1049	1015	981	1141	3287
1177	1235	965	1150	1049	1073	1047	992	1164	3297
1186	1270	1230	1192	1112	1359	1358	1064	1356	
1438	1293	1420	1215	1213	1436	1422	1232	1411	
1451	1461	1431	1232	1283	1446	1436	1371	1418	
1458	1493	1451	1362	1379	1449	1470	1392	1490	
1484	1499	1456	1489	1428	1470	1476	1469	1492	
1502	1508	1528	1508	1484	1501	1709	1487	1506	
3091	2400	3105	1744	1624	3029	3055	1572		
3110	3037	3140	2980	3151	3096	3116	3077		
3190	3045	3254	3066	3201	3124	3141	3151		
3209	3113	3265	3086	3233	3173	3194	3183		
3269	3189	3313	3192	3300	3281	3276	3195		
3285	3197	3320	3253	3305	3292	3292	3300		

Table S4 Energies, frequencies and rotational constants along the entrance channel leading to vdW1 formation

Energy relative to the C(³ P) + CH ₃ OCH ₃ asymptote, (uncorrected for ZPE differences) calculated at the DLPNO-CCSD(T) / AVTZ level / kJ mol ⁻¹																						
vdW1																						C(³ P) + CH ₃ OCH ₃
	-63.5	-60.2	-49.0	-37.5	-28.1	-20.7	-15.4	-12.1	-9.3	-7.0	-5.3	-4.1	-3.4	-2.8	-2.6	-2.2	-2.0	-1.7	-1.4	-1.2	-1.0	-0.7
Distance of approach between C(³ P) and O atom of CH ₃ OCH ₃ / Å																						
	1.65	1.85	2.05	2.25	2.45	2.65	2.85	3.05	3.25	3.45	3.65	3.85	4.05	4.25	4.45	4.65	4.85	5.05	5.25	5.45	5.65	6.05
Frequencies calculated at the M06-2X / AVTZ level / cm ⁻¹																						
	153																					
	239	235	171	170	125	75	119	61	36	83	89	80	57	30	19	37	18	35	16	25	11	10
	328	262	236	197	159	116	170	115	82	134	111	101	76	73	25	64	48	54	45	46	41	33
	347	290	248	239	229	204	208	186	215	226	220	219	210	222	219	221	218	216	215	214	213	213
	387	320	311	304	283	259	257	253	267	287	286	280	274	271	270	269	267	266	264	266	264	264
	506	430	425	427	428	425	430	430	430	432	434	434	431	431	430	432	430	430	429	429	428	428
	917	941	954	963	970	973	976	979	978	981	981	981	980	984	983	984	984	984	984	984	984	984
	1091	1113	1125	1132	1135	1135	1134	1135	1139	1138	1138	1137	1135	1141	1141	1141	1141	1141	1141	1141	1141	1141
	1168	1170	1173	1172	1170	1169	1170	1169	1174	1175	1176	1178	1173	1174	1173	1175	1174	1174	1174	1173	1173	1173
	1207	1212	1213	1213	1208	1202	1202	1201	1204	1207	1207	1209	1203	1204	1203	1204	1203	1203	1203	1203	1203	1203
	1215	1214	1220	1224	1227	1228	1230	1232	1233	1235	1234	1234	1235	1236	1237	1238	1238	1238	1239	1239	1240	1240
	1279	1282	1283	1283	1282	1280	1280	1279	1280	1280	1281	1281	1280	1281	1281	1281	1281	1280	1280	1280	1280	1280
	1455	1460	1463	1463	1463	1462	1465	1462	1463	1463	1463	1463	1460	1464	1464	1465	1464	1465	1464	1464	1464	1465
	1475	1482	1487	1491	1493	1490	1492	1489	1492	1492	1494	1494	1492	1494	1494	1493	1493	1494	1494	1494	1494	1495
	1489	1492	1495	1497	1498	1496	1496	1496	1498	1495	1498	1496	1494	1497	1497	1498	1497	1498	1497	1498	1498	1498
	1494	1496	1497	1498	1500	1500	1501	1501	1503	1503	1503	1507	1502	1504	1505	1504	1504	1504	1504	1504	1505	1505
	1497	1500	1507	1508	1506	1503	1506	1505	1504	1505	1508	1508	1505	1506	1506	1506	1506	1506	1507	1506	1507	1506
	1513	1512	1511	1512	1512	1515	1520	1517	1518	1519	1520	1523	1513	1519	1520	1521	1521	1522	1522	1522	1523	1522
	3069	3058	3047	3037	3029	3023	3019	3016	3012	3013	3012	3010	3012	3007	3006	3009	3005	3011	3008	3011	3009	3011
	3074	3063	3052	3042	3034	3029	3026	3023	3019	3021	3020	3019	3020	3015	3012	3015	3012	3018	3015	3019	3016	3019
	3156	3138	3120	3104	3091	3082	3076	3072	3064	3069	3067	3065	3065	3059	3057	3059	3055	3061	3058	3062	3059	3063
	3157	3139	3123	3107	3095	3086	3081	3076	3070	3073	3072	3070	3071	3065	3064	3066	3062	3068	3065	3069	3066	3068
	3203	3193	3183	3174	3167	3164	3162	3160	3157	3160	3159	3158	3158	3155	3155	3156	3157	3156	3156	3156	3157	3156
	3206	3195	3185	3176	3168	3165	3163	3161	3158	3162	3162	3162	3162	3157	3157	3157	3158	3157	3158	3157	3158	3157
Rotational constants calculated at the M06-2X / AVTZ level / cm ⁻¹																						
A	0.32	0.31	0.31	0.31	0.31	0.30	0.30	0.30	0.30	0.30	0.30	0.30	0.30	0.31	0.31	0.31	0.31	0.32	0.31	0.32	0.32	0.32
B+C	0.24	0.23	0.21	0.19	0.17	0.16	0.15	0.14	0.13	0.12	0.11	0.11	0.10	0.09	0.08	0.08	0.07	0.07	0.06	0.06	0.06	0.05

Table S5 Reactions involved in CH₃OCH₃ production and destruction

	Reaction	ΔE kJ /mol	α	β	γ	F_0	g	ref
1.	CH ₃ + CH ₃ O → CH ₄ + H ₂ CO → CH ₃ OCH ₃	-348 -328	4.0e-11 1.37e-12	0 -0.96	0 0	1.6 10	0 0	(Tsang & Hampson 1986b), (Tennis <i>et al.</i> 2021)
2.	CH ₃ + CH ₃ OH ₂ ⁺ → CH ₃ OHCH ₃ ⁺ + H → CH ₃ CH ₂ OH ₂ ⁺ + H	+45 +12						
3.	CH ₃ OH ₂ ⁺ + CH ₃ OH → CH ₃ OHCH ₃ ⁺ + H ₂ O	-59	1.1e-10	-1.0	0	1.60	0	(Anicich 2003)
4.	CH ₃ ⁺ + CH ₃ OH → CH ₃ OHCH ₃ ⁺ + hν → CH ₄ + H ₂ COH ⁺	-335 -249	7.8e-12 2.3e-9	-1.1 -0.5	0 0	10 1.8	0 0	(Jarrold <i>et al.</i> 1986, Herbst 1987) (Anicich 2003)
5.	NH ₃ + CH ₃ OHCH ₃ ⁺ → CH ₃ OCH ₃ + NH ₄ ⁺	-58	1.0e-9	0	0	1.8	0	(Skouteris <i>et al.</i> 2019)
6.	CH ₃ OHCH ₃ ⁺ + e ⁻ → CH ₃ OCH ₃ + H → CH ₃ OH + CH ₃ → CH ₄ + O + CH ₃	-529 -610 -235	8.5e-8 9.2e-7 7.5e-7	-0.7 -0.7 -0.7	0 0 0	1.6 1.6 1.6	0 0 0	(Hamberg <i>et al.</i> 2010)
7.	H ⁺ + CH ₃ OCH ₃ → CH ₃ OCH ₃ ⁺ + H → CH ₄ + H ₂ COH ⁺	-356 -693	2.5e-9 2.5e-9	-0.5 -0.5	0 0	3 3	0 0	By comparison with H ⁺ + H ₂ CO, CH ₃ OH but without introducing CH ₃ OCH ₂ ⁺ .
8.	He ⁺ + CH ₃ OCH ₃ → CH ₂ ⁺ + CH ₃ O + H + He → CH ₃ ⁺ + H + H ₂ CO + He → HCO ⁺ + CH ₃ + H ₂ + He	-585 -1082 -1205	7e-11 4e-10 6e-10	0 0 0	0 0 0	1.6 1.6 1.6	0 0 0	(Ascenzi <i>et al.</i> 2019)
9.	H ₃ ⁺ + CH ₃ OCH ₃ → CH ₃ OHCH ₃ ⁺ + H ₂ → CH ₃ OH + CH ₃ ⁺ + H ₂ → CH ₄ + CH ₃ ⁺ + H ₂ O → CH ₃ OH + CH ₅ ⁺ → H ₂ COH ⁺ + CH ₄ + H ₂ → CH ₃ OCH ₂ ⁺ + H ₂ + H ₂ → C ₂ H ₅ ⁺ + H ₂ O + H ₂	-354 -18 -126 -195 -267 -236 -244	5.6e-10 4.2e-10 9.4e-10 3.8e-10 1.2e-9 0(7.1e-10) 4.7e-10	-0.5	0	1.8	0	(Lee <i>et al.</i> 1992) CH ₃ OCH ₂ ⁺ not included in our network.
10.	C ⁺ + CH ₃ OCH ₃ → C + CH ₃ OCH ₃ ⁺ → CH ₃ + CH ₃ CO ⁺ → CH ₃ ⁺ + CH ₃ CO	-140 -806 -537	2.0e-9 2.0e-9 0	-0.5 -0.5	0 0	2 2	0 0	Rate constant and products guessed by comparison with C ⁺ + CH ₃ OH, (CH ₃) ₂ CO (Anicich 2003).
11.	C + CH ₃ OCH ₃ → CH ₃ + CH ₃ + CO	-345	1.3e-11	-1.0	0	1.4	8	50-300K, this work (we do not consider CH ₃ OC formation included into CH ₃ + CH ₃ + CO channel). We use k=1.3e-10 cm ³ .s ⁻¹ in the 10-49K range.
12.	OH + CH ₃ OCH ₃ → CH ₃ OCH ₂ + H ₂ O	-94	1.0e-11	0	0	2	0	Around 10-50K only. (Shannon <i>et al.</i> 2014a, Klippenstein 2017)

13.	$\text{HCO}^+ + \text{CH}_3\text{OCH}_3 \rightarrow \text{CH}_3\text{OHCH}_3^+ + \text{CO}$		2.1e-9	-0.5	0	1.4	0	(Anicich 2003)
14.	$\text{S}^+ + \text{CH}_3\text{OCH}_3 \rightarrow \text{S} + \text{CH}_3\text{OCH}_3^+$	-54	1.0e-9	-0.5	0	1.6	0	(Decker <i>et al.</i> 2000) with simplified products.
15.	$\text{Cl} + \text{CH}_3\text{OCH}_3 \rightarrow \text{HCl} + \text{CH}_3\text{OCH}_2$	-31	1.80e-10	0	0	1.4	0	(Jenkin <i>et al.</i> 2010)

	Reaction	ΔE kJ/mol	Branching ratio	γ (K)	Ref
16.	$\text{C} + \text{s-CH}_3\text{OH} \rightarrow \text{s-CH}_3\text{OCH}$ $\rightarrow \text{s-CH}_4 + \text{s-CO}$ $\rightarrow \text{s-CH}_3\text{CHO}$	-396 -691 -672	0.2 0.5 0.3	0 0 0	This reaction have been studied in the gas phase being barrierless and leading mostly to $\text{CH}_3 + \text{HCO}$ through CH_3OCH intermediate formation (Shannon <i>et al.</i> 2014b). On Ice some CH_3OCH will be stabilized and $\text{CH}_3 + \text{HCO}$ should give CH_3CHO and $\text{CH}_4 + \text{CO}$ as CH_3 and HCO will stay close on Ice. This reaction may also produce some $\text{C}_2\text{H}_3\text{OH}$ and $\text{c-C}_2\text{H}_4\text{O}$.
17.	$\text{s-H} + \text{s-CH}_3\text{OCH} \rightarrow \text{s-CH}_3\text{OCH}_2$ $\rightarrow \text{s-C}_2\text{H}_5\text{O}$ $\rightarrow \text{s-CH}_3 + \text{s-H}_2\text{CO}$	-334 -346 -288	0.5 0.5 0	0 0	The TS for $\text{CH}_3\text{OCH}_2 \rightarrow \text{C}_2\text{H}_5\text{O}$ is located 207 kJ/mol above the CH_3OCH_2 energy, so -126 kJ/mol below the entrance level. Some CH_3OCH_2 may dissociate into $\text{CH}_3 + \text{H}_2\text{CO}$.
18.	$\text{s-H} + \text{s-CH}_3\text{OCH}_2 \rightarrow \text{s-CH}_3\text{OCH}_3$ $\rightarrow \text{s-CH}_4 + \text{s-H}_2\text{CO}$	-401 -383	1 0	0	The TS for $\text{CH}_3\text{OCH}_3 \rightarrow \text{CH}_4 + \text{H}_2\text{CO}$ is located 479 kJ/mol above the CH_3OCH_3 energy, so CH_3OCH_3 cannot dissociate.
19.	$\text{s-HCO} + \text{s-CH}_3\text{OCH}_2 \rightarrow \text{s-CH}_3\text{OCH}_3 + \text{s-CO}$	-332	1	0	We neglect $\text{CH}_3\text{OCH}_2\text{CHO}$ formation which is however likely not negligible.
20.	$\text{s-H} + \text{s-CH}_3\text{OCH}_3 \rightarrow \text{s-CH}_3\text{OCH}_2 + \text{s-H}_2$ $\rightarrow \text{s-CH}_3 + \text{s-CH}_3\text{OH}$	-25 -98	1 0	4040 (1550i) ?	This work (M06-2X/AVTZ level) in good agreement with (Takahashi <i>et al.</i> 2007) who obtain a barrier height equal to 4090 K.
21.	$\text{s-CH}_3\text{O} + \text{s-CH}_3\text{OCH}_3 \rightarrow \text{s-CH}_3\text{OCH}_2 + \text{s-CH}_3\text{OH}$	-35	1	1900(1200i)	This work (M06-2X/AVTZ level)
22.	$\text{s-CH}_2\text{OH} + \text{s-CH}_3\text{OCH}_3 \rightarrow \text{s-CH}_3\text{OCH}_2 + \text{s-CH}_3\text{OH}$	0	0	7900(1730i)	This work (M06-2X/AVTZ level)
23.	$\text{s-CH}_3 + \text{s-CH}_3\text{O} \rightarrow \text{s-CH}_3\text{OCH}_3$ $\rightarrow \text{s-CH}_4 + \text{s-H}_2\text{CO}$	-345 -336	0.9 0.1	0 0	Gas phase branching ratio of (Tsang & Hampson 1986a) favor H atom abstraction but not for the study of (Enrique-Romero <i>et al.</i> 2022) on Ice reactions where CH_3O and CH_2OH are not good H donor. The TS for $\text{CH}_3\text{OCH}_3 \rightarrow \text{CH}_4 + \text{H}_2\text{CO}$ is located 479 kJ/mol above the CH_3OCH_3 energy, so CH_3OCH_3 cannot dissociate.

Anicich V.G., 2003, JPL Publication-03-19, Pasadena, CA, USA,

Ascenzi D., Cernuto A., Balucani N., Tosi P., Ceccarelli C., Martini L.M., Pirani F., 2019, Astronomy and Astrophysics, 625, A72

Decker B.K., Babcock L.M., Adams N.G., 2000, Journal of Physical Chemistry A, 104, 801

Enrique-Romero J., Rimola A., Ceccarelli C., Ugliengo P., Balucani N., Skouteris D., 2022, The Astrophysical Journal Supplement Series, 259, 39

Hamberg M., et al., 2010, A&A, 522, A90

Herbst E., 1987, ApJ., 313, 867
Jarrold M.F., Kirchner N.J., Liu S., Bowers M.T., 1986, The Journal of Physical Chemistry, 90, 78
Jenkin M.E., Hurley M.D., Wallington T.J., 2010, The Journal of Physical Chemistry A, 114, 408
Klippenstein S.J., 2017, Proceedings of the Combustion Institute, 36, 77
Lee S.H., Drucker M., Adams N.G., 1992, International Journal of Mass Spectrometry and Ion Processes, 117, 101
Shannon R.J., Caravan R.L., Blitz M.A., Heard D.E., 2014a, Physical Chemistry Chemical Physics, 16, 3466
Shannon R.J., Cossou C., Loison J.-C., Caubet P., Balucani N., Seakins P.W., Wakelam V., Hickson K.M., 2014b, RSC Advances, 4, 26342
Skouteris D., Balucani N., Ceccarelli C., Faginas Lago N., Codella C., Falcinelli S., Rosi M., 2019,
Takahashi K., Yamamoto O., Inomata T., Kogoma M., 2007, International Journal of Chemical Kinetics, 39, 97
Tennis J., Loison J.-C., Herbst E., 2021, The Astrophysical Journal, 922, 133
Tsang W., Hampson R.F., 1986a, Journal of Physical and Chemical Reference Data, 15, 1087
Tsang W., Hampson R.F., 1986b, J. Phys. Chem. ref. Data, 15, 1087